Modelling and analysis of floating spar-type wind turbine drivetrain

Published in:
Wind Energy

Document Version:
Peer reviewed version

Queen's University Belfast - Research Portal:
Link to publication record in Queen's University Belfast Research Portal

RESEARCH ARTICLE

Modelling and analysis of floating spar-type wind turbine drivetrain

Y. Xing[1], M. Karimirad[1,2], T. Moan[1,2]

[1] Centre for Ships and Ocean Structures, Norwegian University of Science and Technology, 7491 Trondheim, Norway

[2] Norwegian Research Centre for Offshore Wind Technology, Norwegian University of Science and Technology, 7491 Trondheim, Norway

ABSTRACT

This paper deals with the drivetrain dynamics study of a 750 kW spar-type floating wind turbine (FWT). The drivetrain studied is a high-speed generator, one-stage planetary, two stage parallel and three-point support type. The response analysis is carried out in two steps. First, global aero-hydro-elastic-servo time-domain analyses are performed using HAWC2. The main shaft loads, which include the axial forces, shear forces and bending moments, are obtained in this integrated wind-wave response analysis. These are then used as inputs for the multibody drivetrain time-domain analyses in SIMPACK. The investigations are largely based on comparisons of the main shaft loads and internal drivetrain responses from one-hour simulations. The tooth contact forces, bearing loads and gear deflections are the internal drivetrain response variables studied. The comparisons are based on the mean values, standard deviations and maximum values extrapolated using a 10^{-5} up-crossing rate. Both operational and parked conditions are considered. The investigation proceeds in three parts. First, the responses are compared between the FWT and its equivalent land-based version. Second, the contributions from the main shaft loads (shear forces, axial forces and bending moments) and nacelle motions are individually investigated. Third, an improved four-point support (4PT) system is studied and compared against the original three-point support (3PT) system for the FWT. The results show that there are general increases in the standard deviations of the main shaft loads and internal drivetrain responses in the FWT. In addition, it was found that these increases are a result of the increased main shaft loads in the FWT, especially the non-torque loads. Lastly, the 4PT system when applied to a FWT drivetrain significantly reduces the tooth contact forces and bearing loads in the low-speed stage, but this comes at the expense of increased main bearing radial loads. Copyright © 2012 John Wiley & Sons, Ltd.

Correspondence

Y. Xing, Centre for Ships and Ocean Structures, Norwegian University of Science and Technology, 7491 Trondheim, Norway.

Tel.: +47 73 59 5567, Fax: +47 73 59 55 28, Email: yihan.xing@ntnu.no

1. INTRODUCTION

There have been plans, in recent years, to exploit offshore wind energy on a large scale. There are large sea areas with stronger and steadier wind as compared to land sites. This is a good motivation for the wind industry to move towards offshore wind. However, most of the offshore wind resource potential in many countries are found at water depths above 60 m [1]. It is costly to use fixed structures to mount wind turbines for the deeper water depths [2]. It is, therefore, of vital interest to explore the use of floating platforms for mounting wind turbines to harness these wind resources that are available at deep waters. These systems are termed as floating wind turbines (FWTs). A FWT is specifically designed to produce power from offshore wind resources in intermediate to deep waters. There have been various FWT concepts proposed in recent years. These include the spar, semi-submersible and tension-leg platform concepts. Understanding the response characteristics of the FWT system under environmental conditions is important for its design, operation and survival. The design of the FWT demands coupled time domain analysis that considers aerodynamic, hydrodynamics, structural dynamics and control systems [3].

The spar-type FWT, which is the same concept as the Statoil's Hywind spar [4] and the OC3 spar [5], is studied in this paper. This concept is currently the most well studied FWT with numerous aero-hydro-elastic-servo response analyses performed [3, 6, 7, 8, 9]. Furthermore, the Statoil Hywind spar has been built to full scale and installed in southern Norway. These previous studies have focused on the global responses. The internal drivetrain dynamics were not considered. On the other hand, there have also been studies on the internal drivetrain dynamics of land-based wind turbines (WTs) in recent years [10, 11, 12, 13, 14, 15, 16, 17, 18, 19, 20, 21]. Studies on FWT drivetrain are lacking in the public domain. Deeper understanding of the FWT drivetrain is crucial in the de-risking of offshore wind turbine designs. The nature of the load effects on a FWT is different as compared to a land-based WT due to the presence of wave-induced responses. The first study on a spar-type FWT drivetrain was performed by Xing et al. [22]. In this paper, the main shaft loads and internal drivetrain responses in terms of the mean values and standard deviation values were compared between the FWT and WT. It was found that there is a general increase in the responses, especially in terms of the standard deviations.

The investigation in this paper is largely based on the comparisons of the main shaft loads and internal drivetrain responses. Both operational and parked load cases are compared in terms of the main shaft loads. Only operational load cases are considered for the internal drivetrain responses. The investigation proceeds in three parts. First, the comparison work in Xing et al. [22] is further extended. Maximum values and frequency spectra are now also compared. More comparisons of the mean values and standard deviations will also be presented. Second, the individual drivetrain inputs (main shaft axial forces, shear forces, bending moments and nacelle motions) are removed one at a time to quantity their
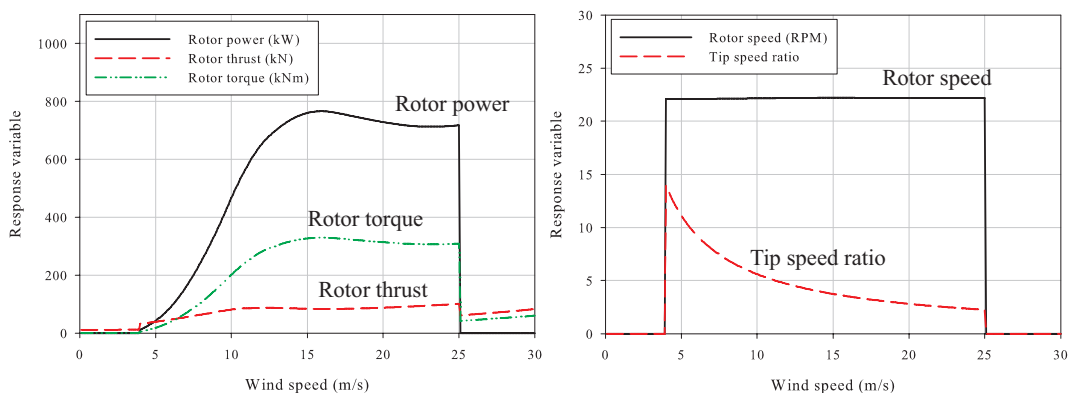
Figure 1. The GRC WT system steady-state characteristics

respective contributions to the internal drivetrain responses. Lastly, an improved four-point support version of the drivetrain system is compared against the original three-point support system for the FWT.

2. SYSTEM DESCRIPTION

The FWT system will be described in two parts: first, the WT system and second, the designed floating system.

2.1. The wind turbine and drivetrain

The WT from the National Renewable Energy Laboratory's (NREL's) Gearbox Reliability Collaborative (GRC) project [23] is used. The GRC WT is a 750 kW stall-regulated, fixed-speed, three-bladed upwind WT. See Figure 1 for the GRC WT steady-state system characteristics. The WT is parked above the cut-out wind speed of 25 m/s. The GRC gearbox has one planetary stage, two parallel stages, and uses the three-point support system. The input and output shafts are not co-axial. Its topology is similar to those of the larger conventional MW gearboxes seen today. The GRC drivetrain and gearbox are shown in Figure 2. The gearbox topology with the naming convention for each individual bearing is presented in Figure 3. INP-A (spherical roller bearing) is the main shaft bearing. PLC-A and PLC-B (full complement cylindrical roller bearings) are the planet carrier bearings. PL-A and PL-B (cylindrical roller bearings) are the planet gear bearings. LS-SH-A & LS-SH-B & LS-SH-C, IMS-SH-A & IMS-SH-B & IMS-SH-C and HS-SH-A & HS-SH-B & HS-SH-C are the low-, intermediate- and high-speed stage bearings respectively. The upwind bearings, i.e. A, in these stages are cylindrical roller bearings, while the downwind bearings, i.e. B and C are tapered roller bearings. The B and C bearings, therefore, carry the axial forces acting on the shafts in this bearing set-up. This is also a floating sun system that allows for better load sharing between the three planet gears in the low-speed planetary stage.
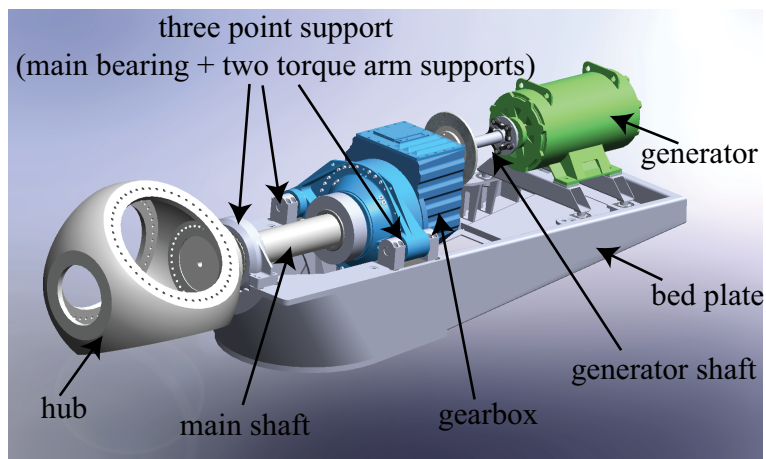
Figure 2. The GRC WT drivetrain and gearbox
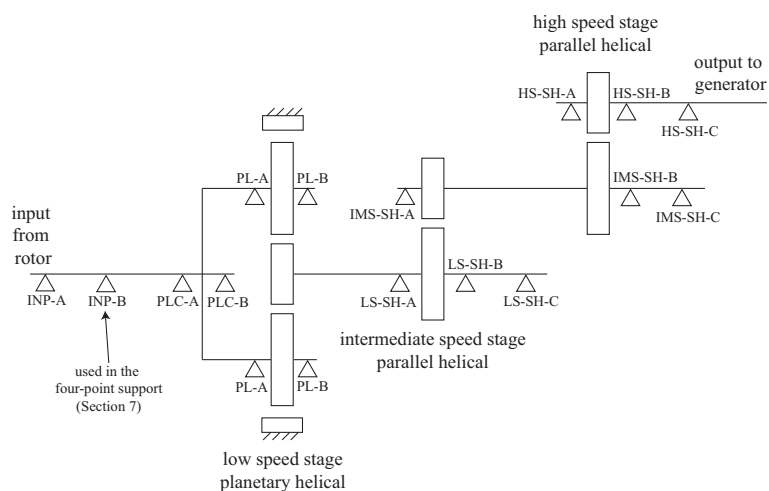
Figure 3. The GRC gearbox topology

2.2. The floating spar system

A spar-type FWT system was designed for the GRC WT for the purpose of producing realistic loading conditions for the GRC drivetrain. The system's schematic and main characteristic parameters are presented in Figure 4 and Table I respectively. This is a catenary moored spar system that uses three mooring lines with fairleads located on the spar circumference. The main purpose of the mooring lines is station-keeping in surge and sway. The delta mooring layout provides extra yaw stiffness and the clumped weights increase the pre-tension in the mooring lines. The pitch and roll motions of this FWT system are primarily ballast-stabilised. This is provided by the large roll and pitch hydrostatic restoring moments due to the low centre of gravity. There are no yaw hydrodynamic excitation forces. The wind, however, does excite the system in yaw. There are also some yaw excitations due to the rotor gyroscopic effect, but these are relatively

small. There are limited motions in heave due to the small water plane area and deep draft. The draft and diameter of the spar were selected to achieve below a 5-degree static pitch displacement at 150 per cent maximum aerodynamic thrust. The natural periods in heave, roll and pitch are designed to be above 20 seconds, i.e. above the wave peak periods. The yaw natural period is designed to be below five seconds, i.e. below the wave peak periods. Special care has been applied to avoid Mathieu instability by ensuring that the ratio between the heave and roll/pitch natural periods are not in the ratios of 0.5, 1, 1.5, 2.0, etc. [24].

Simo/Riflex [25, 26], in combination with an external simplified aerodynamic thrust calculation dynamic linked library (DLL), has been used extensively for the design of this FWT system. Simo/Riflex is developed by Marintek and has been widely applied to perform coupled response analysis of moored offshore structures under hydrodynamic loading. Simo solves the hydrodynamic multibody problem, while Riflex solves the mooring line problem using a FE approach. The external DLL calculates the aerodynamic thrust loading at the hub as a function of the thrust coefficient and the relative wind velocities the hub experiences. The coupling of Simo/Riflex/external DLL, therefore, solves the coupled wave-wind induced FWT dynamic problem. It has been shown that this method is sufficient for obtaining accurate global responses [27]. This method has also been applied for the global response analyses of spar, semi-submersible and tension-leg type FWTs [27, 28, 29]. This simplified DLL, however, can only provide accurate rotor thrust loads. The Simo/Riflex/external DLL method was used to calculate the dynamic responses of the designed FWT at all the load cases presented in Table II. The global responses were checked for all these load cases under different unidirectional wave and wind headings from 0 to 90 degrees. Different headings are required as the incoming wind and wave are asymmetrical to the three-line mooring layout except at angular intervals of 60 degrees. This asymmetrical heading induces coupled roll-pitch-yaw motions. The mooring load distributions for each individual line were also checked.

3. THEORY AND METHODOLOGY

A two-step decoupled analysis approach is applied to the FWT drivetrain. First, global aero-hydro-elastic-servo analyses are performed in HAWC2 [30] to obtain the loads and motions on the drivetrain. Second, these loads and motions are then used as inputs into a multibody drivetrain model in SIMPACK [31]. HAWC2 is a full-fledged aeroelastic code developed by DTU Wind, Denmark. It is more refined, but also significantly more computationally expensive than the Simo/Riflex/external DLL approach used in the design of the FWT system (Section 2.2). The HAWC2 model provides main shaft loads in all six degrees of freedom (dofs), i.e. shear forces, axial forces, bending moments and torques, which cannot be captured using the Simo/Riflex/external DLL approach. SIMPACK is a multi-purpose multibody simulation
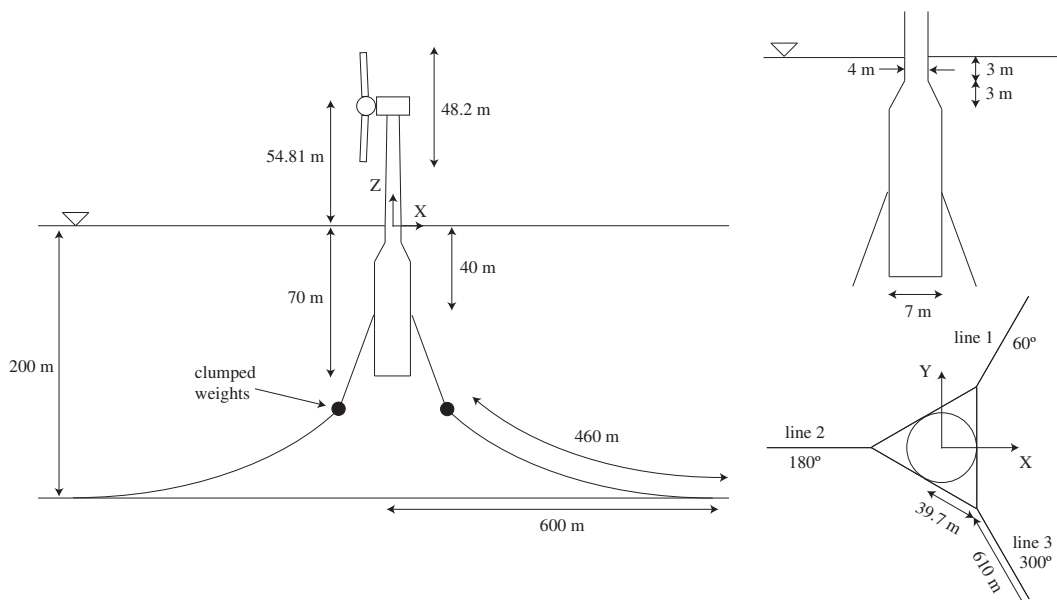
Figure 4. The floating spar system for the GRC wind turbine

Table I. The floating wind turbine (entire system) characteristics.

Mass, excluding mooring lines	2.6381×10^6 kg
Centre of buoyancy, CB	-36.5 m
Centre of gravity, CG	-40.1 m
Roll/pitch inertia about CG	7.4809×10^8 kg.m^2
Yaw inertia about CG	1.7633×10^7 kg.m^2
Clumped weight mass	10 000 kg
Surge/sway natural periods	105.1 s
Heave natural period	29.5 s
Roll/pitch natural periods	21.0 s
Yaw natural period	4.7 s

code with features available to model gearboxes. See Figure 5 for an illustration of the application of these loads and motions on the drivetrain model. The main shaft loads, i.e. forces and moments, are applied at the end of the main shaft where the rotor hub is connected. The nacelle motions are applied on a dummy body where the drivetrain is placed on.

This decoupled approach does not consider the effect of the feedback forces of the gearbox on the rotor. The feedback forces from the gearbox should be relatively small. This is because the gearbox has eigenfrequencies that are much higher

Figure 5. Application of calculated loads and motions on the drivetrain model. The torque arms and housing casings are not shown.

compared to the wind turbine structure. The first drivetrain eigenmode, which is of relatively lower frequency, is however included in the HAWC2 model through a single degree-of-freedom (DOF) torsional spring-damper system. This single DOF spring-damper system models the feedback of the drivetrain dynamics on the global aero-hydro-elastic-servo model.
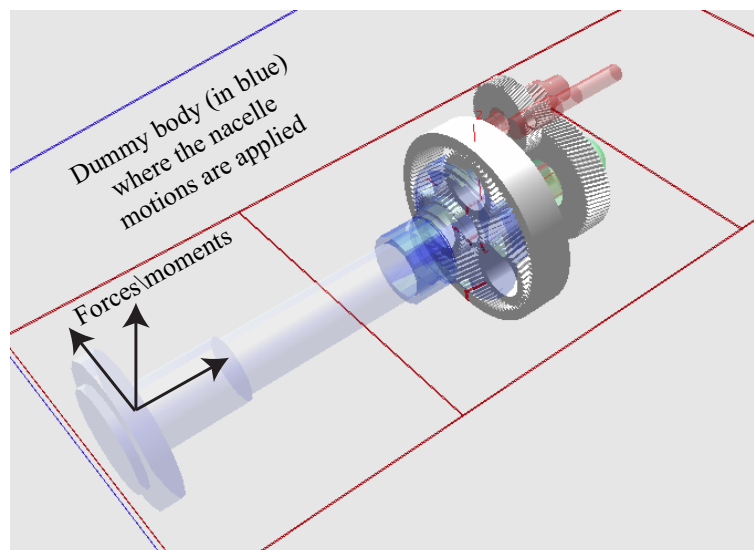
The theory and methodology of the global aero-hydro-elastic-servo analysis, the multibody simulation of the drivetrain model, the environmental conditions applied and the extreme value estimation used in this paper are discussed further in the following sub-sections.

3.1. Global aero-hydro-elastic-servo floating wind turbine simulation using HAWC2

In HAWC2, the FWT/WT structure is modelled using multibodies consisting of Timoshenko beam elements. The deflections are small and linear within a body [30, 32]. Large deflections, i.e. geometrical nonlinearity, can be considered by using the geometrical substructuring technique. This means to model a component, e.g. the blade, using several bodies. Further details on the geometrical substructuring technique and its application to beams can be found in Xing et al. [33] and Wu et al. [34].

The aerodynamic loads are calculated using the blade element momentum method with various engineering corrections that account for dynamic inflow, dynamic stall, skew inflow, shear effects on induction and effects from large deflections. For example, the MHH Beddoes method [35] is used as the dynamic stall model and the Prandtl tip loss [36] model is applied to account for tip loss. Aerodynamic drag on the tower and nacelle is also included. Tower shadow effects are also

accounted for. The potential flow method is used to describe the tower shadow as it is, in the case for an upwind turbine, better than a jet model [30].

The hydrodynamic loads are calculated using the Morison formula [37]. This formulation is well suited for slender structures where the spar diameter is much smaller than the wave length. The floating spar platform, studied in this paper, is in this category. According to the Morsion formula, the hydrodynamic loads acting at a strip along the length of the slender structure is given by

$$dF = \frac{\rho}{2}C_d D |u_r| u_r + \rho \frac{\pi D^2}{4} C_a \dot{u}_r + \rho \frac{\pi D^2}{4} \dot{u}_w. \tag{1}$$

$u_r = u_w - u_b$ is the relative velocity of the strip in water, u_w is the water velocity at the strip, u_b is the body velocity at the strip, C_d is the drag coefficient, C_a is the added mass coefficient and D is the strip diameter. The first term in the equation is the quadratic viscous drag, the second term consists of the diffraction and added mass forces and the last term is the Froude-Krylov force. This formulation considers the instantaneous position of the spar. The mass and drag coefficients depend on the Kaulegan-Carpenter number, which is about five for this floating spar system. This gives an added mass coefficient of 1.0 and drag coefficient of 0.6 for smooth cylinders. These are applied in this work. The Morison formula does not provide heave excitation and buoyancy forces. These are accounted separately in HAWC2 using a simplified pressure integration method. Details of this can be found in Karimirad et al. [38].

The mooring lines are modelled using force elements implemented as DLLs. The mooring forces are represented using a quasi-static force model that utilises the two-dimensional load-displacement relationships. This model accounts for the coupling of the mooring lines in the surge/pitch and sway/roll directions, but neglects the inertia and damping effects of the mooring system. This assumption is valid as the mass of the mooring lines is small as compared to the spar platform. The damping of the mooring lines is due to the viscous forces they experienced. These forces have limited contributions to the global responses of the spar floater. Furthermore, this model does not provide any information on the mooring line tension distribution. See Figure 6 for the mooring surge force and pitch moment when the spar is displaced in the surge and pitch directions. These mooring relationships are obtained from Simo/Riflex static calculations.

The generator model, which is a Thevenin generator, is implemented as a force element DLL. The generator torque-speed curve is presented in Figure 7. In addition, as mentioned in the Section 3, the drivetrain is modelled in the FWT/WT structure using a single DOF torsional spring-damper system.
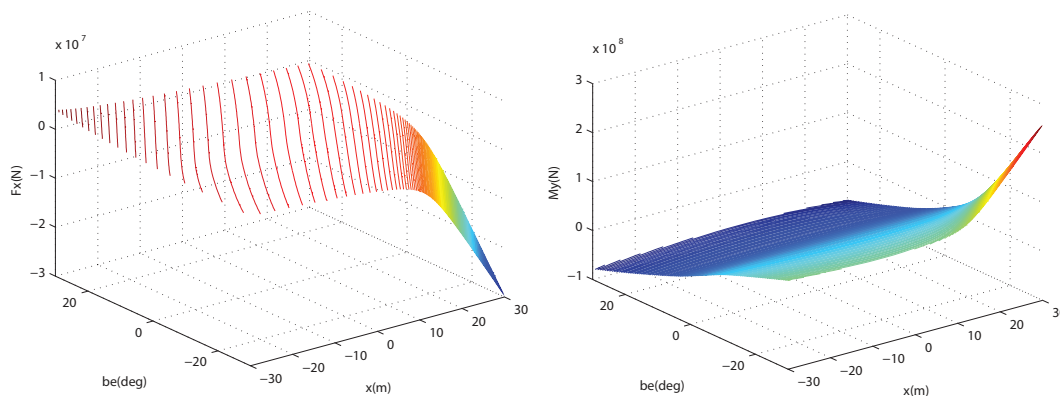
Figure 6. Two-dimensional load-displacement relationships for the surge force and pitch moment when the FWT is displaced in the

surge and pitch directions. be = pitch angle of spar.
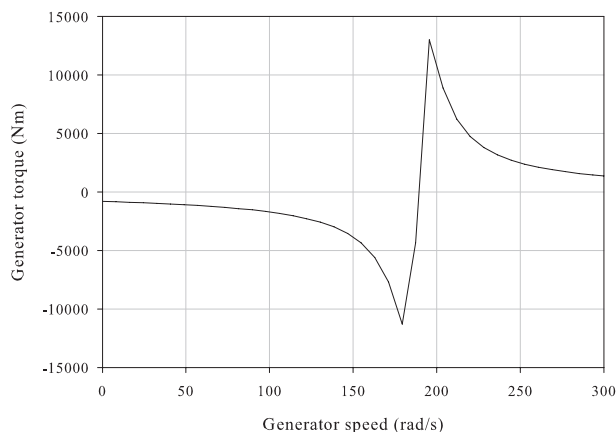
Figure 7. The GRC Thevenin generator torque-speed curve

3.2. Multibody simulation of the drivetrain using SIMPACK

In SIMPACK, each component of the drivetrain is modelled as a rigid or flexible body, and interconnected using joints, force elements and constraints. Model fidelity study of the same FWT drivetrain under environmental loads was performed previously in Xing et al. [22]. The study concluded that a drivetrain model that utilises six dofs rigid gear wheels with tooth compliance, bearing compliance and flexible shafts was sufficient to produce accurate results for the mean values and standard deviations of most internal drivetrain response variables. The results of this model fidelity study are presented in the Appendix. This level of model detail is, therefore, used in this paper. The SIMPACK model topology diagram of the drivetrain is presented in Figure 8 (Only one planet gear is shown for ease of understanding). As an example to explain the connection sequence, the connection of the planet gear to other bodies in the model topology will briefly described here. The planet gear is connected to the planet pin through a six-degree of freedom joint and two force elements that model the

bearings (PL-A and PL-B). The planet gear is also connected to the ring and sun gears through force elements that model

the tooth contact forces. A proportional-integral velocity controller is applied at the end of the high-speed shaft to model

the generator. This velocity controller uses the generator speed obtained from the HAWC2 simulations as reference, and

calculates the generator torque, T as:

$$T = K_P \left(\omega - \omega_{ref} \right) + K_I \int_0^t \left(\omega - \omega_{ref} \right) \mathrm{d}t \tag{2}$$

where $\omega - \omega_{ref}$ and $\int_0^t \left(\omega - \omega_{ref} \right) \mathrm{d}t$ are the speed error and integral speed error, respectively. ω is the generator speed,

ω_{ref} is the reference generator speed, K_P is the proportional gain, K_I is the integral gain and t is the current simulation

time. The proportional gain of the controller is chosen to be the gradient of the slip-slope of the Thevenin generator model

used in the global aero-hydro-elastic servo analyses (see Figure 7). Using the same proportional gain as the gradient of the

slip-slope means that the velocity controller is, in fact, the original Thevenin generator model. The integral gain is chosen

to minimise the steady-state speed error. In general, these chosen proportional and integral gains will result in a maximum

speed error of 0.5 rad/s in the generator speed in the simulations performed in this paper. The input main shaft loads

are applied at the hub connection end of the main shaft. The nacelle motions are modelled as prescribed displacements,

velocities and accelerations at the joint of the dummy body. It was previously mentioned that Figure 5 illustrates the

application of loads and motions on the drivetrain model. The tooth compliance is modelled using SIMPACK's gear pair

element, FE225. FE225 models gear contact as a series of discrete springs and dampers. The gear stiffness is calculated

in accordance with ISO 6336-1 [39]. This stiffness parameter depends on the location of the contact point and the gear

geometry. The forces and torques acting on each individual gear are calculated as a function of the gear stiffness and the

penetration depth at the gear teeth. FE225 also considers normal damping, coulomb friction, backlash and micro-geometry.

The bearings are modelled as force elements using diagonal linear stiffness matrices with clearances considered.

The following response variables are studied: (i) tooth contact forces, (ii) bearing forces and (iii) gear deflections. There

are obviously many other interesting response variables that can be studied, but the study here will be limited to this

handful of response variables.

3.3. Environmental conditions

The Statfjord site is used as a representative site for the FWT installation. This is an oil and gas field that is operated by

Statoil in the Norwegian sector of the North Sea, and located at 59.7N and 4.0E, 70 km from the shore. Simultaneous wind

and wave measurements were taken at this site from 1973 to 1999, and the data smoothed and empirically fitted [40]. This

is used to correlate the wind and wave in the load cases studied in this paper. The load cases are presented in Table II, and
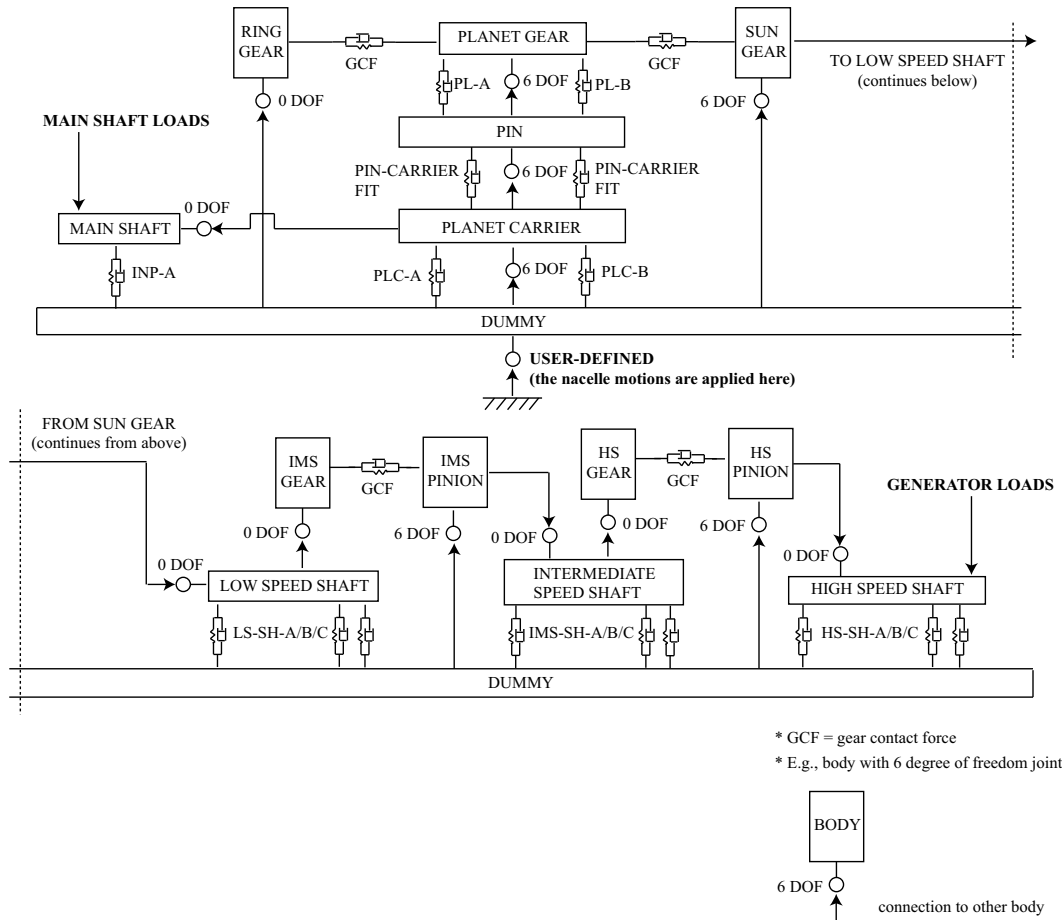
Figure 8. The SIMPACK model topology diagram of the drivetrain. Note that the presentation of the model is separated into two parts.

cover a range of operating and parked conditions. It is also to be noted there are currently no IEC standards for FWTs and the current IEC standards for offshore wind turbines, IEC 61400-3 [41], apply only to offshore bottom-fixed WTs. The selected load cases are meant to be generalised operating and survival conditions. A more complete range of load cases should be considered in future research work, but is out of the scope of this paper. The fitting formulae for the expected significant wave height, $E(H_S)$ (m) and expected wave peak period, $E(T_P)$ (s) as a function of the mean ten minute wind speed at ten metres, V (m/s) are

$$E(H_S) = \beta \Gamma(\frac{1}{\alpha} + 1) \tag{3}$$

where $\alpha = 2 + 0.135V$ and $\beta = 1.8 + 0.1V^{1.322}$, and

$$E(T_P) = (4.882 + 2.68H_s^{0.529}) \left(1 - 0.19 \frac{V - (1.764 + 3.426H_s^{0.78})}{1.764 + 3.426H_s^{0.78}} \right). \tag{4}$$

Table II. The load cases used in this study. LC = load case number, V_{mean} = mean wind speed at hub height (10-min), H_S = significant wave height, T_P = wave peak period and I = wind turbulent intensity.

LC	V_{mean} (m/s)	H_S (m)	T_P (s)	I	Status
1	42.5	10.1	13.1	0.1	Parked
2	30	6.9	11.8	0.1	Parked
3	25	5.7	11.3	0.1	Parked
4	20	4.7	10.8	0.11	Operating
5	16	3.9	10.4	0.12	Operating
6	12	3.1	10.1	0.13	Operating
7	8	2.5	9.8	0.15	Operating

A ten-per cent increase in the mean wind speed is used to scale a one-hour mean wind speed to a ten-minute one [9]. Furthermore, the power law (using a power coefficient of 1/7) is applied to scale the wind speed at the ten-metre height to the wind speed at hub height.

Linear wave theory (Airy theory) is applied together with wheeler stretching to describe the wave kinematics. The Joint North Sea Wave Project (JONSWAP) wave spectrum is used to represent the long-crested irregular waves. The spectrum is given as:

$$S_{JS}(f) = \frac{1}{5(0.065\gamma^{0.803} + 0.135)} \cdot S_{PM}(f) \cdot exp\left(\frac{-(f - f_P)}{2\sigma^2 f_P^2}\right). \tag{5}$$

The unit of $S_{JS}(f)$ is m^2/s. f is the wave frequency (Hz), γ is the shape factor, $S_{PM}(f)$ is the Pierson Moskowitz spectrum (m^2/s), σ is a constant that relates to wind speed and fetch length and f_p is the peak wave frequency (Hz). $\gamma = 3.3$, representing a developing sea is used. It is mentioned that $\gamma = 1.0$ represents a fully developed sea. Values of $\sigma = 0.07$ when $f <= f_P$ and $\sigma = 0.09$ when $f > f_P$ are also used. Refer to Faltinsen [37] for more detailed explanations on wave environment modelling.

The Mann uniform shear turbulence model is used to generate the turbulent wind field. This model assumes that the isotropic von Karman energy spectrum is distorted rapidly by an uniform, mean velocity shear. A three-dimensional velocity spectral tensor is also defined, making it unique from other models. Further details of this model can be found in Mann [42, 43]. Class C, which is dedicated to offshore wind turbines is used to define the turbulent intensity.

3.4. Extreme value estimation

The extreme value is the maximum in a set of finite number of independent and identically distributed random variables. Extreme value statistics for responses over a certain time period, e.g. one or three hours, can be calculated by using the regularity of the tail region of the mean up-crossing rate. The up-crossing of high response values are statistically independent events [44], and thus a Poisson probability distribution is assumed for the extreme values. The cumulative distribution function for a response variable is then given by

$$P(Y(T) <= y) = exp\left(-\int_0^T \upsilon_y^+(t)dt\right) \qquad (6)$$

where υ_y^+ is the positive up-crossing rate of the level y. The up-crossing rate of a process at a defined level is the frequency of passing that level. For example, an up-crossing rate of 10^{-4} at a defined level means that the response passes this defined level at a frequency of 0.0001 Hz. The up-crossing rate is lower for high response levels. υ_y^+ is found from time-domain simulations, and extrapolation is required for low values of up-crossing rates. The extrapolation strategy proposed by Naess et al. [44] is used. In this strategy, the mean up-crossing rate is extrapolated based on Monto Carlo simulations, i.e. time-domain simulations of stochastic realisations. The up-crossing rate is assumed to be in the following form:

$$\upsilon_y^+(y) = q(y)exp\left(a(y-b)^c\right), \qquad (7)$$

where $q(y) = q\,exp(\delta(y) + d(y))$ is slowly varying compared to $exp\left(a(y-b)^c\right)$. This assumption was derived from the observation that the tail of the mean up-crossing rate for a wide range of dynamical systems behaves with good approximation like $exp\left(a(y-b)^c\right)$. Plotting $log(log(\upsilon_y^+(y)/q))$ against $log(y-b)$ would give a nearly linear tail behaviour under the assumptions made. Appropriate values for q and b are then chosen to optimise this linear fit. The reader is referred to Naess et al. [44] for a detailed explanation of this method.

See Figure 9 for an example of the extrapolation of the INP-A bearing axial forces in the LC4 case (Table II). The corresponding Poisson distributions for the maxima values with different up-crossing rates indicated are also illustrated in the same figure. The area under the Poisson curve, the fractal, up to the different up-crossing rates are also indicated. Observe that up-crossing rates of 10^{-4}, 10^{-5} and 10^{-6} give about 36%, 91% and 99% fractal respectively. Observe also that an up-crossing of 10^{-4} gives a maximum value that is close to the most probable maximum. The maximum values presented in this paper (Sections 5 - 7) are obtained using five one-hour simulations and extrapolated with a up-crossing rate of 10^{-5}.
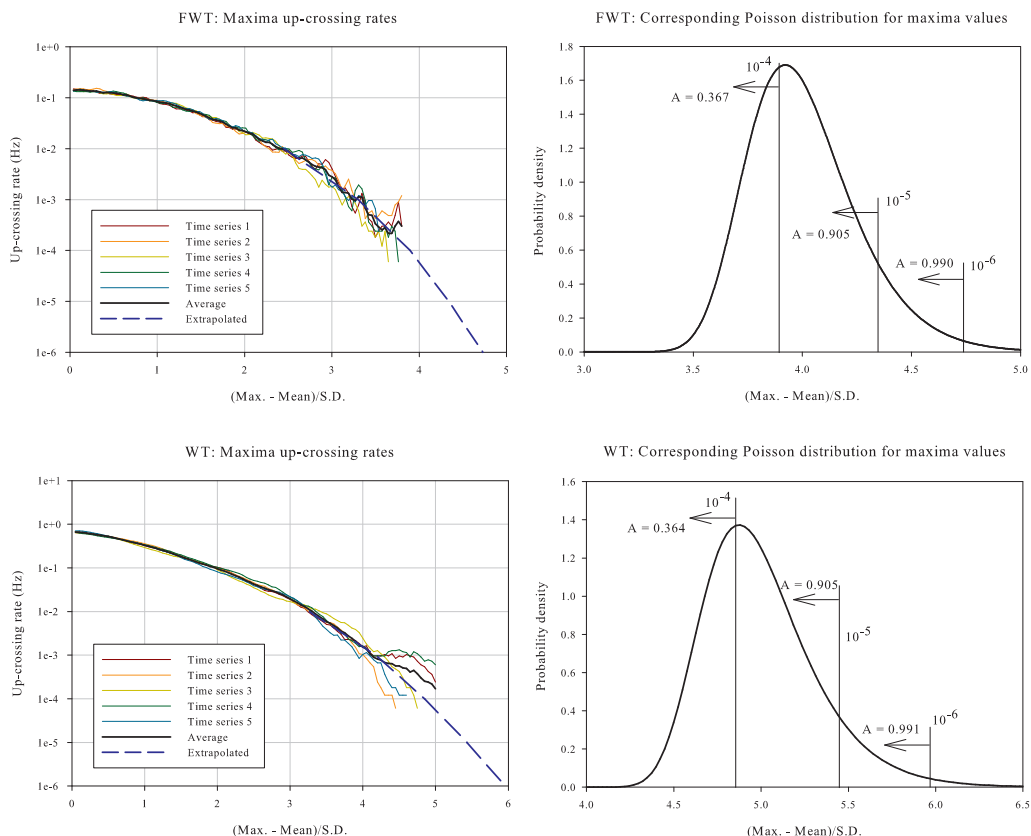
Figure 9. 1st row: FWT. 2nd row: WT. Left: Extrapolation of up-crossing rate for the INP-A bearing axial forces in the LC4 case. Right: Equivalent Poisson distribution with up-crossing rates indicated. A = area.

4. FLOATING WIND TURBINE GLOBAL RESPONSE CHARACTERISTICS

Unidirectional wind and waves directed along the positive x-axis in the global frame (Figure 4) are considered in this paper. Figure 10 presents the statistical responses of the most important nacelle motions (surge and pitch) experienced under the different load cases. The results are based on one-hour simulations calculated using HAWC2. Figure 11 presents the frequency spectra of the nacelle surge and pitch motions in the LC4 case. As observed in these frequency spectra, the maxima occur at the wave peak period. This means that the standard deviations of nacelle motions are primarily wave induced. The mean values, on the other hand, are primarily wind-induced [8].

5. COMPARISONS OF RESPONSES, FWT VERSUS WT

The mean values and standard deviations of the main shaft loads and internal drivetrain responses of the FWT and WT were compared in Xing et al. [22]. It was found that there is a general increase in the main shaft loads and internal drivetrain
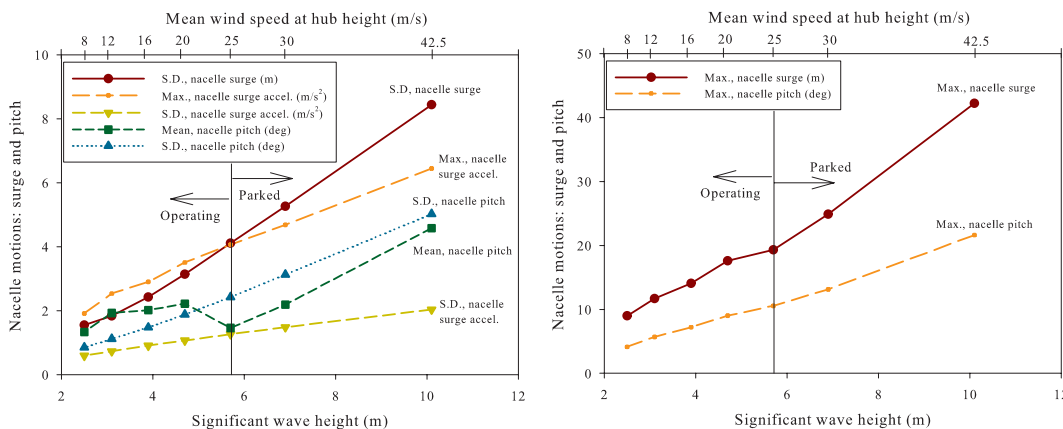
Figure 10. FWT nacelle motions at different load cases. Results are based on one hour simulations.
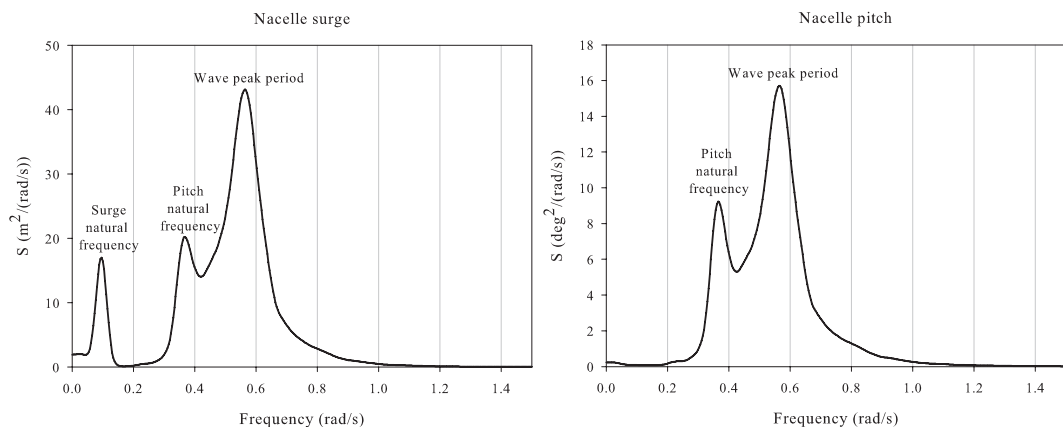
Figure 11. Frequency spectra of nacelle surge and pitch in the LC4 case, based on one-hour simulations.

responses for the FWT, especially in terms of standard deviations. These increases in load and responses appear mainly in the responses associated with the low speed planetary stage, but do propagate to the intermediate and high speed stages at the less severe load cases. The comparisons are extended in this section to the maximum values and frequency spectra. Note that none of the maximum values from the LC6 and LC7 load cases are higher than the LC4 and LC5 load cases. This means a higher percentage increase in a particular response value in the LC6/LC7 load case as compared to the LC4/LC5 load case is not critical. It is, therefore, important to focus on the LC4 and LC5 load cases when comparing the maximum values.

5.1. Comparisons of main shaft loads

The comparisons of the main shaft loads at different load cases are presented in Figure 12. The results are presented as the percentage differences of the FWT response value versus the WT response value, i.e.

$$\%difference = \frac{X_{FWT} - X_{WT}}{X_{WT}} \times 100\%. \tag{8}$$

The comparisons of the main shaft loads frequency spectra of the FWT and WT at the LC4 case are presented in Figure 13.

There are up to 20 per cent increases in the mean values and standard deviations of the bending moments and torques in the FWT. In general, these differences increase with increasing severity of the load case. Note that the absolute values of the standard deviations of the axial and shear forces in the WT are small, and thus the percentage differences appear to be large, i.e. above 100 percent. The standard deviations in the axial forces range from 13.3 - 42.5 kN and 3.2 - 20.2 kN for the FWT and WT, respectively. While the standard deviations in the shear forces range from 1.7 - 7.5 kN and 0.4 - 1.6 kN for the FWT and WT, respectively.

The maximum values of the main shaft loads are significantly higher in the FWT, with the exception of the maximum shear forces. The maximum axial loads are especially higher; as much as above 80 per cent higher when the wind speed is 25 m/s. The maximum bending moments are the largest at the most severe operational load case, i.e. LC4, which are about 40 per cent higher in the FWT. The maximum torques are larger in the less and more severe load cases during operational and parked conditions respectively. The larger maximum torques at the less severe operational load cases can be attributed to the larger standard deviations in the torques experienced as the turbulent wind intensities are higher at lower wind speeds.

The comparisons of the frequency spectra show that the extra contributions in the FWT case are mainly wave-induced as they are primarily associated with the wave excitation frequencies and the platform natural frequencies, i.e. platform heave and pitch. This means that the increases in the standard deviations of the main shaft loads in the FWT are mainly wave-induced. Note that the horizontal axes are in logarithmic scale. This means that the differences in the low frequency part are visually exaggerated, and therefore, any big differences in the frequency spectra of the main shaft in this region are in fact small. Also note that since the standard deviations of the shear forces are small, the increase in the area in the frequency spectrum of the FWT shear forces in Figure 13 is also in fact small.
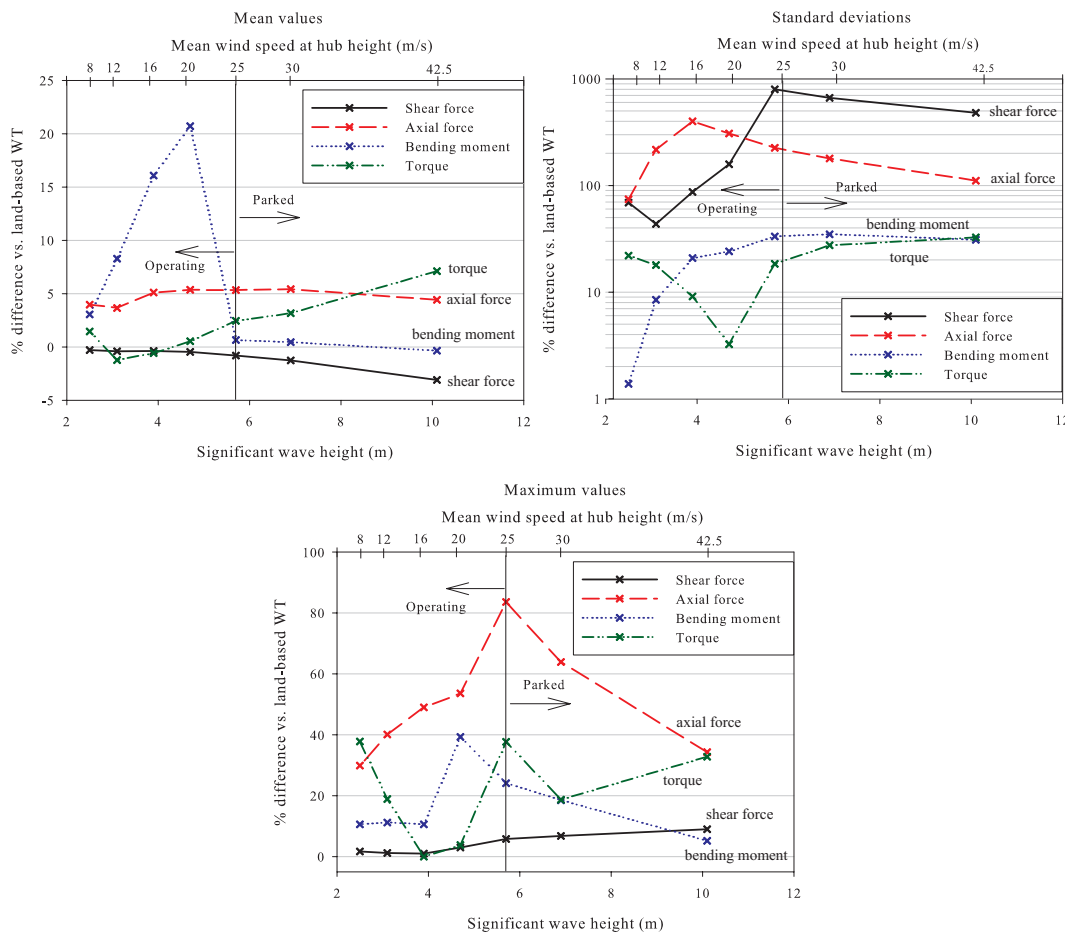
Figure 12. Comparisons of mean values, standard deviations and maximum values of main shaft loads, FWT = floating wind turbine, WT = land based wind turbine.

5.2. Comparisons of internal drivetrain responses

In this section, the comparisons of the internal drivetrain responses are presented. The results are presented in Tables III - V as the percentage differences versus the WT responses (see Equation 8). The comparisons of the frequency spectra of the Sun-Planet & Planet-Ring gear contact forces, the bearing loads of INP-A, PLC-B & PL-B and the gear deflections of the sun & planet gears are presented in Figures 14 - 16 respectively. Results from only one planet gear are presented, even though there are a total of three planet gears in this system. It is also mentioned that tooth contact forces mean the total integrated tooth contact forces along the tooth flank.

The comparisons show that increases in standard deviations appear in many of the response variables. These appear mainly in the response variables associated with the low-speed planetary stage, but also in the variables associated with the intermediate- and high-speed stages at less severe load cases. Increases in maximum values, on the other hand, appear
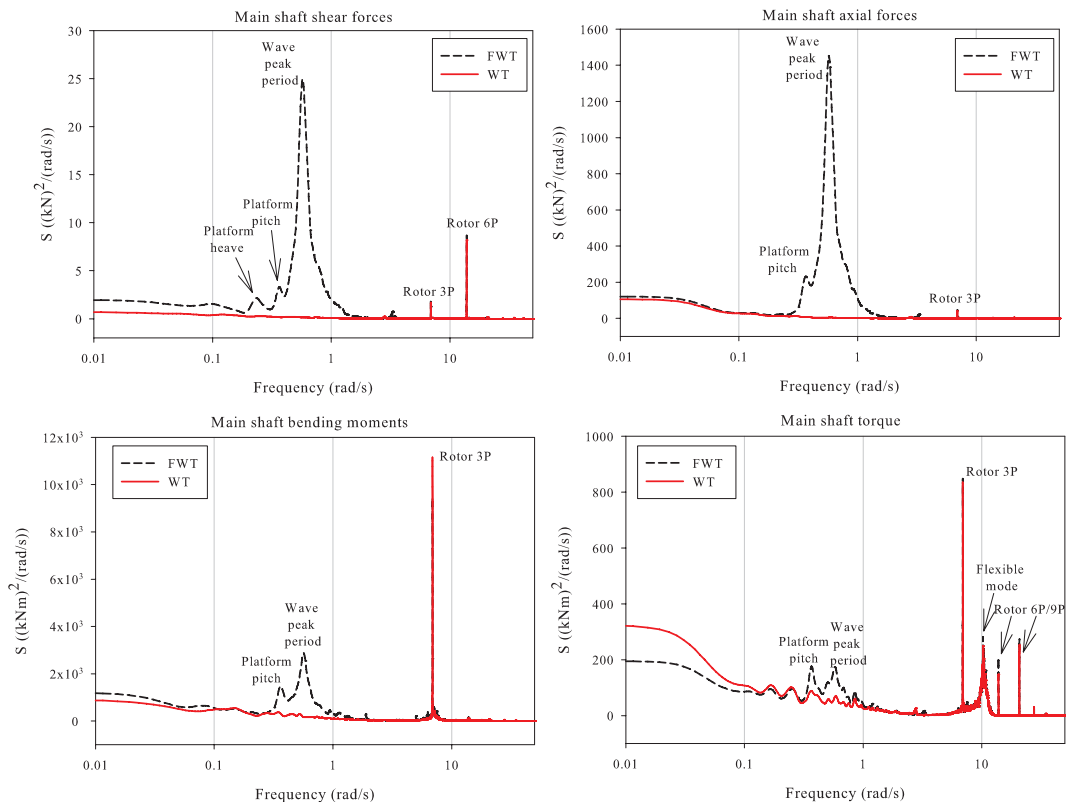
Figure 13. Comparisons of frequency spectra of the axial force, shear force, bending moment and torque on the main shaft in the LC4 case.

mainly in the bearing loads in the low-speed planetary stage. This is intuitive as the majority of the increase in the main shaft loads as presented in Section 5.1 should be carried by the low-speed stage as the gearbox has the ability to isolate loads between the individual gear stages. The increase in standard deviations is an indication of increased fatigue loads. However, this has to be validated by fatigue damage calculations in future research work. Comparisons of the frequency spectra reveal that wave induced responses appear in the FWT internal drivetrain responses. This suggests that the increases in standard deviations are wave-induced. There are also some increases in the mean values of bearing loads and planet gear axial displacements.

Tooth contact forces   There are no differences in the mean tooth contact forces. On the other hand, there are increases in the standard deviations of the tooth contact forces. These increases are, in general, larger at less severe load cases. This goes along with the trend of the standard deviations of the main shaft torques as presented in Figure 12. There are no significant increases in the maximum tooth contact forces in the LC4 and LC5 load cases.

Table III. FWT vs. WT. Comparisons of tooth contact forces. Mean values, standard deviations and maximum values.

Gear pair	%difference vs. WT											
	Mean				S.D.				Max.			
	LC4	LC5	LC6	LC7	LC4	LC5	LC6	LC7	LC4	LC5	LC6	LC7
LSS-Sun-Planet	0.51	-0.58	-1.17	1.48	8.30	14.02	20.26	22.10	2.80	1.33	0.86	9.15
LSS-Planet-Ring	0.51	-0.58	-1.17	1.49	8.43	14.13	20.27	22.10	4.34	1.30	0.75	12.02
IMSS	0.51	-0.58	-1.19	1.51	3.53	12.06	19.88	22.32	5.35	1.51	1.29	12.83
HSS	0.52	-0.58	-1.18	1.52	2.72	9.30	18.51	21.77	4.30	2.02	1.38	13.14
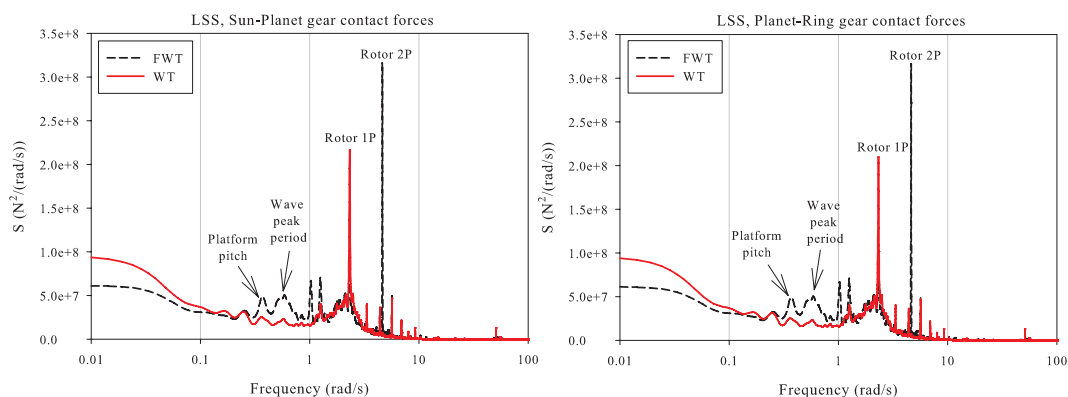
Figure 14. FWT vs. WT. Comparisons of frequency spectra of the Sun-Planet and Planet-Ring gear contact forces in the LC4 case.

Bearing loads   There are general increases in the standard deviations of the bearing loads associated with the low speed planetary stage. These increases also appear at the intermediate- and high-speed stages at the less severe load cases. Interestingly, there are decreases in the mean radial loads of the INP-A bearing and tilting moments of the LS-SH-A, LS-SH-B & LS-SH-C bearings. There are also huge increases in the INP-A, PLC-B & PL1-B maximum axial bearing loads, PLC-A, PLC-B & LS-SH-A maximum radial bearing loads and INP-A & PLC-B maximum tilt bearing loads.

Gear deflections   There are general increases in the axial gear displacements. There are decreases in the tilting displacements of the sun and intermediate-speed stage gears. There are limited differences in the radial and tilting gear displacements of most gears.

Prepared using weauth.cls

Table IV. FWT vs. WT. Comparisons of bearing loads. Mean values, standard deviations and maximum values. Refer to Figure 3 for bearing notation.

Bearing	%difference vs. WT											
	Mean				S.D.				Max.			
	LC4	LC5	LC6	LC7	LC4	LC5	LC6	LC7	LC4	LC5	LC6	LC7
	Axial forces											
INP-A	6.21	5.93	4.47	4.67	387.99	548.48	298.20	90.16	66.21	70.60	55.52	36.63
PLC-B	6.77	6.26	4.89	4.87	405.94	504.98	297.02	92.26	68.62	62.38	56.81	39.42
PL-B	41.65	36.87	35.91	26.31	34.04	28.60	27.61	15.41	12.26	8.42	4.29	10.56
LS-SH-B	-0.46	-1.46	-2.22	-0.12	5.36	12.31	19.79	21.98	1.59	-1.52	0.04	11.83
LS-SH-C	-0.45	-1.46	-2.22	-0.11	5.37	12.32	19.80	21.98	1.40	-1.43	-0.57	10.97
IMS-SH-B	0.15	-0.88	-1.59	0.90	1.80	7.37	17.04	21.31	2.41	0.05	-0.88	11.83
IMS-SH-C	0.15	-0.89	-1.59	0.90	1.80	7.34	17.02	21.29	2.91	-0.55	-1.48	10.79
HS-SH-B	0.38	-0.70	-1.33	1.30	0.67	3.27	13.11	20.35	1.02	0.19	-0.72	13.70
HS-SH-C	0.38	-0.71	-1.34	1.29	0.64	3.17	12.94	20.29	1.01	0.96	-0.58	14.40
	Radial forces											
INP-A	-15.57	-16.15	-16.09	-17.87	22.86	25.56	26.15	26.68	4.49	2.42	1.83	2.20
PLC-A	33.49	32.47	50.63	16.59	35.85	25.27	29.73	11.43	39.75	14.60	18.37	9.87
PLC-B	44.29	-11.42	7.34	25.27	41.16	0.12	9.22	23.79	37.42	10.75	2.91	8.43
PL-A	0.57	-0.51	-1.14	1.64	12.90	6.83	10.72	10.46	6.80	5.83	8.10	13.62
PL-B	0.73	-0.46	-1.01	1.31	12.54	7.38	12.96	13.67	3.33	4.20	7.36	14.07
LS-SH-A	-1.36	8.67	5.36	5.10	46.15	39.07	25.02	8.56	14.27	7.04	2.38	1.41
LS-SH-B	4.22	3.00	0.99	5.99	-8.83	-10.15	12.26	18.33	2.14	-0.02	0.98	10.24
LS-SH-C	-5.26	-9.87	-7.50	-4.35	24.63	23.60	1.20	13.66	1.84	2.06	3.76	17.15
IMS-SH-A	-0.06	-1.39	-1.58	0.69	1.75	5.68	13.47	20.58	0.17	0.41	-0.22	7.91
IMS-SH-B	0.88	-0.28	-1.20	4.38	3.36	9.87	19.81	19.85	4.07	0.32	1.94	13.47
IMS-SH-C	1.17	0.99	0.05	-0.27	1.29	2.42	13.10	23.06	0.65	-1.10	1.81	5.66
HS-SH-A	0.40	-0.48	-1.10	0.42	2.24	8.41	19.16	23.22	1.11	1.89	3.66	8.16
HS-SH-B	2.57	-1.64	2.31	-1.36	2.15	-0.35	4.04	10.04	4.45	4.49	2.46	97.48
HS-SH-C	0.18	-0.35	2.06	6.59	1.09	-0.11	6.69	16.13	5.80	-0.03	1.12	22.27
	Tilting moments											
INP-A	13.45	8.69	13.50	3.85	29.02	17.09	15.73	5.67	14.23	11.04	12.79	6.82

Table V. FWT vs. WT. Comparisons of gear deflections. Mean values, standard deviations and maximum values.

| Gear	%difference vs. WT											
	Mean				S.D.				Max.			
	LC4	LC5	LC6	LC7	LC4	LC5	LC6	LC7	LC4	LC5	LC6	LC7
	Axial displacements											
LSS-Sun	-0.20	-1.24	-1.99	0.27	3.49	11.95	19.95	22.07	1.12	-2.19	-0.79	13.79
LSS-Planet	42.71	37.84	36.64	26.42	34.07	28.58	27.62	15.37	11.28	8.10	1.82	10.95
IMSS-gear	-0.50	-1.51	-2.26	-0.16	5.29	12.28	19.67	21.96	1.58	-2.41	-0.65	10.27
IMSS-pinion	0.15	-0.88	-1.59	0.90	1.79	7.40	17.05	21.33	1.41	0.56	-2.81	12.08
HSS-gear	0.13	-0.90	-1.60	0.87	1.79	7.20	16.84	21.25	1.59	0.53	-1.80	11.71
HSS-pinion	0.38	-0.69	-1.32	1.27	0.71	3.52	13.52	20.53	1.37	-1.07	-0.10	14.49
	Radial displacements											
LSS-Sun	-10.54	-4.50	-1.14	-3.12	36.00	21.80	7.71	-3.33	13.58	6.86	1.29	0.80
LSS-Planet	-0.08	-0.33	-0.54	-0.17	1.73	1.30	5.35	10.39	2.07	0.09	-0.47	3.65
IMSS-gear	5.86	6.49	4.10	3.42	-7.10	-5.29	-3.34	-3.27	0.99	0.00	-0.83	-0.81
IMSS-pinion	0.05	-0.42	-0.49	0.03	0.40	1.57	6.52	9.58	1.74	-0.16	1.17	4.10
HSS-gear	-0.05	-0.73	-0.73	0.14	0.48	1.28	5.28	9.02	2.01	-0.50	1.46	5.94
HSS-pinion	0.15	-0.19	-0.54	-1.09	0.33	0.86	8.02	22.98	1.12	0.94	1.04	4.03
	Tilting displacements											
LSS-Sun	-11.91	-14.28	-7.58	-10.55	0.79	-3.51	-5.17	-12.97	8.95	1.81	2.08	-0.21
LSS-Planet	5.97	3.11	4.34	4.84	5.54	3.68	4.73	2.44	5.84	2.60	-0.26	-0.27
IMSS-gear	-39.61	-40.03	-32.05	-26.76	-9.08	-8.43	-10.08	-14.57	6.79	4.18	1.86	0.45
IMSS-pinion	0.93	2.06	1.38	-0.33	0.21	-0.51	-0.70	1.68	0.00	0.00	4.55	4.76
HSS-gear	0.42	0.49	0.12	-0.23	0.40	0.25	0.31	4.34	3.32	2.27	5.56	2.32
HSS-pinion	-0.01	0.01	-0.31	-2.23	0.17	-0.16	1.00	23.67	-0.98	0.00	0.00	0.00

Prepared using weauth.cls
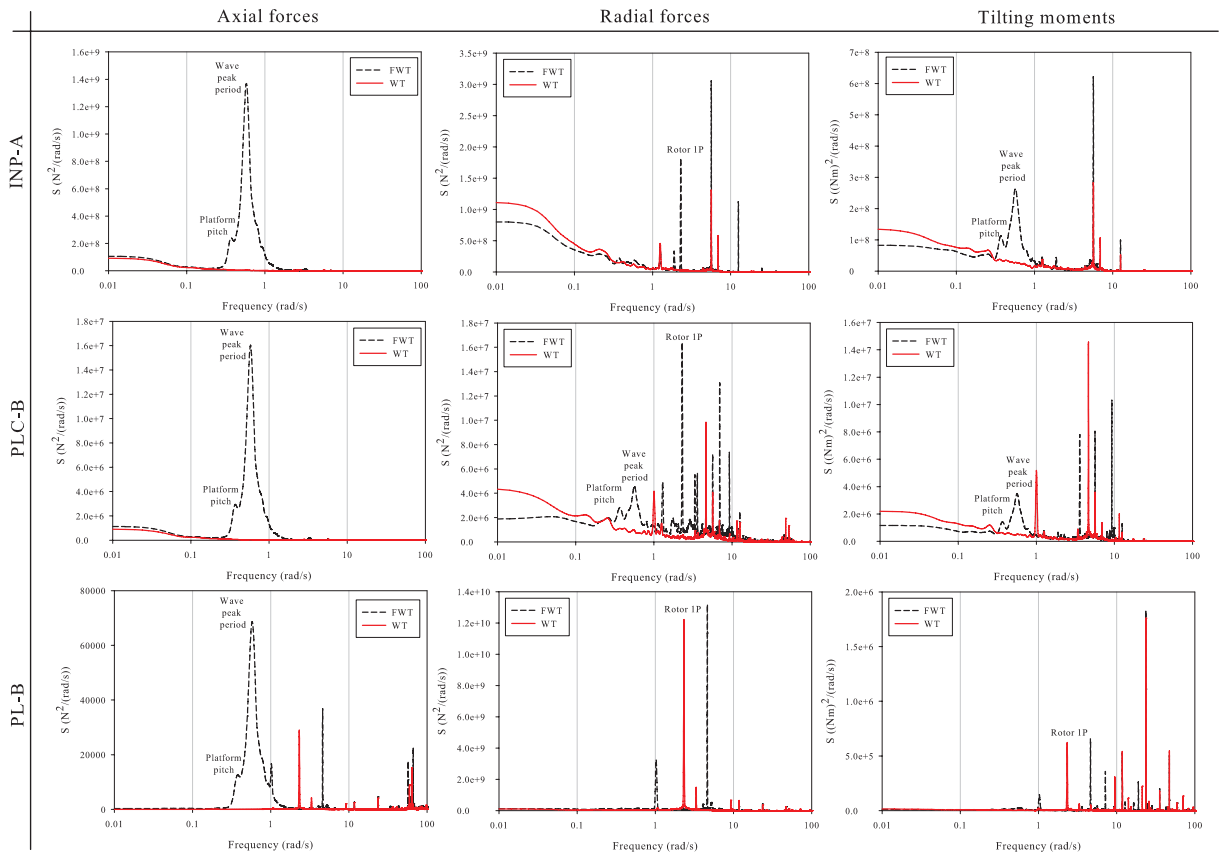
Figure 15. FWT vs. WT. Comparisons of frequency spectra of the INP-A, PLC-B and PL-B bearing loads in the LC4 case.
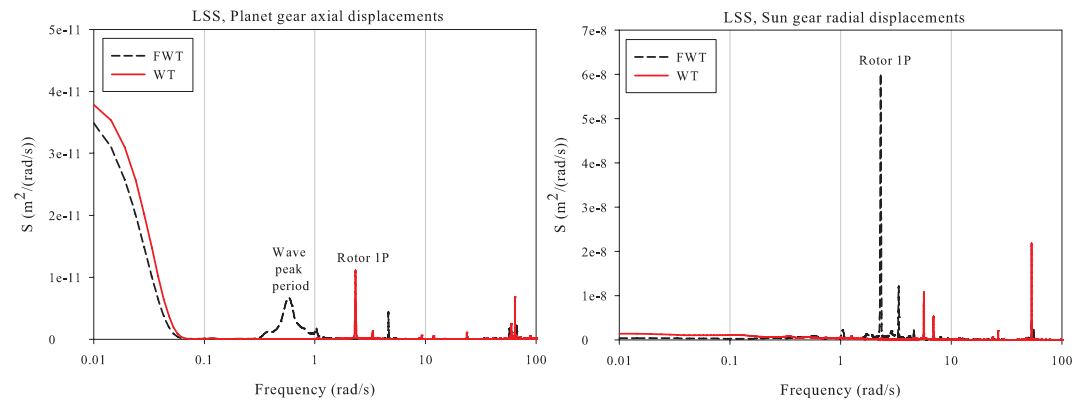

Figure 16. FWT vs. WT. Comparison of frequency spectra of the sun gear radial and planet gear axial displacements in the LC4 case.

6. INVESTIGATING INDIVIDUAL CONTRIBUTIONS TO FWT INTERNAL DRIVETRAIN RESPONSES

In this section, the individual contributions to the FWT internal drivetrain responses are investigated. This is achieved by removing a load component one at a time and comparing the internal drivetrain responses obtained to the base case. The

base case has all the load components are included. These load components are the main shaft non-torque loads, i.e. axial forces, shear forces and bending moments & nacelle motions. Nacelle motions can be understood as inertia loads. The results are presented in Figures 17 - 19 as the percentage differences in the responses versus the base case, i.e.

$$\%difference = \frac{X_{examined\,case} - X_{base\,case}}{X_{base\,case}} \times 100\%. \tag{9}$$

The responses are lower when a load component is not considered, therefore the resulting percentage differences are negative.

The results show that there are, in general, limited differences at the intermediate- and high-speed stages, i.e. the main shaft non-torque loads and nacelle motions have limited contributions in the higher speed stages. Once again, this is intuitive as the gearbox has the capability to isolate loads between the individual stages. The results show that main shaft non-torque loads are very important in predicting accurate internal responses, especially for the bearing loads and gear displacements. Nacelle motions, i.e. inertia forces do not have significant contributions to most response variables, except the bearing axial forces in the planetary stage and planet gear axial displacements. This gives the further conclusion that the differences between the FWT and the WT in the internal drivetrain responses, as presented in Section 5.2, are a result of the differences in the main shaft non-torque loads experienced. A summary of the results is presented in Table VI. In this table, load components that result in a more than 5 percent differences in the internal drivetrain responses when not included are marked with '+'. The most dominating load component, i.e., the component that results in the largest differences in the responses when not included are marked with '++'.

Tooth contact force   The main shaft non-torque loads and nacelle motions have limited contributions to the tooth contact forces. Removing any of the load components do not give rise to more than five per cent decreases in all the tooth contact forces in the gearbox. This means that tooth contact forces are mainly due to the main shaft torques. It is mentioned again that these are the total integrated tooth contact forces. A closer inspection into the comparisons of the face load factors reveal larger differences. The face load factor is the ratio between the maximum tooth contact force and the mean tooth contact force along the tooth flank. The results presented in Figure 17 reveal that the face load factors are heavily influenced by the bending moments in the main shaft. This is as much as minus 40 per cent differences in the standard deviations in the gear teeth in the planetary stage when bending moments are not considered. This is somewhat intuitive as bending in the main shaft misaligns the gears, which leads to higher tooth edge loading. It is also interesting to note that the face load factors of the intermediate-speed gears are also significantly influenced (about minus 20 per cent in standard deviations) by the main shaft bending. The face load factors are also slightly influenced by the main shaft shear forces with about minus

five per cent differences when not considered. It is important that due care be exercised when interpreting the results as the level of drivetrain model fidelity employed here might not be sufficient for the convergence of the face load factors. This is because the misalignment of the gears affects the calculation of the face load factors, and it was previously mentioned in Section 3.2 that a fully flexible, high fidelity model is required for converged gear displacements in Xing et al. [22]. Moreover, for computational reasons, nine gear slices are used per gear contact pair, and this is somewhat not sufficient for a converged face load factor. It was shown in LaCava et al. [45] that 35 gear slices are required for convergence to within 5 per cent. It is mentioned that higher fidelity models were employed in LaCava et al. [45], where the gears can deflect more, and thus might require more gear slices for convergence as compared to the drivetrain model used in this paper. Furthermore, the flexibility of the ring gear can be important, but this was not modelled. More detailed analyses (that employ a high fidelity model) should be performed if an accurate face load factors are required. Nevertheless, the results presented here do provide the insight that the increase in the bending of the main shaft leads to higher face load factors in the planetary stage, even though the total integrated gear contact forces do not appear to be significantly increased.

Bearing loads   The main shaft axial forces have significant contributions to the axial forces of the INP-A and PLC-B bearings. Neglecting the main shaft axial forces results in more than 80 per cent reductions in the axial forces (both mean values and standard deviations) in these bearings. The main shaft bending moments are crucial in the prediction of the bearing radial forces and tilt moments. Neglecting the main shaft bending moments results in large reductions in the bearing radial forces and tilt moments calculated for the planetary stage. On the other hand, the main shaft shear forces are less important to the internal responses in the gearbox. They, however, are crucial to the prediction of the INP-A radial forces. Lastly, nacelle motions have relatively significant contributions to the mean values of the planet bearing axial forces and the standard deviations of the INP-A & PLC-B axial forces.

Gear deflections   Main shaft bending moments are, in general, important in the prediction of the gear displacements. Nacelle motions do also contribute significantly to the planet gear axial displacements.

7. IMPROVING PERFORMANCE WITH A FOUR-POINT SUPPORT DRIVETRAIN

In this section, a four-point support drivetrain system (4PT) will be compared against the original three-point system (3PT) that has been used thus far. The motivation is to improve the performance of the FWT drivetrain by isolating more of the main shaft non-torque loads away from the gearbox. A 4PT has an additional bearing that provides more support to the
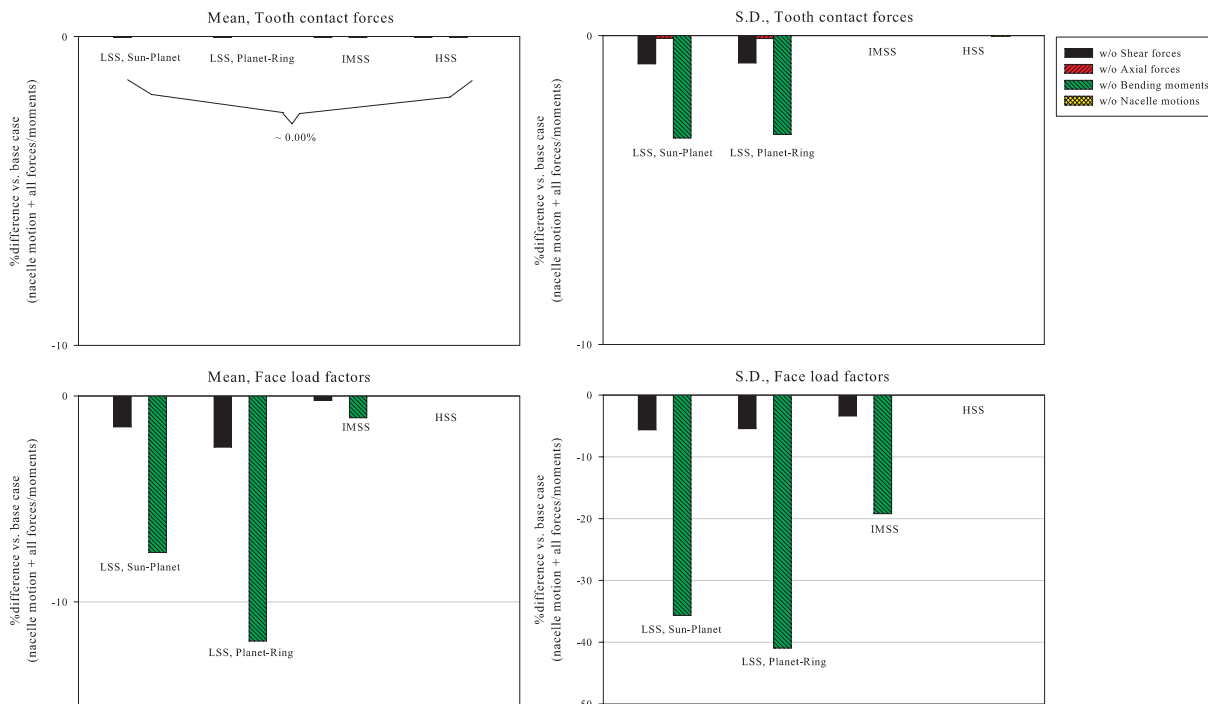
Figure 17. Segregating contributions to the FWT tooth contact forces.

Table VI. Summary of contributions from main shaft non-torque loads and nacelle motions. '+' - load component that results in more than 5 percent differences in the responses when not included. '++' - most dominating load component, i.e., results in the largest differences in the responses when not included.

Type of loading	Contribution						
	Tooth contact forces	Bearing loads			Gear deflections		
		Axial	Radial	Tilt	Axial	Radial	Tilt
Shear forces	+		+	+	+	+	+
Axial forces		++					
Bending moments	++		++	++		++	++
Nacelle motions (inertia forces)		+			++		

main shaft. This causes the shaft to bend less, and thus reduces non-torque loads into the gearbox. This additional bearing, labelled INP-B, is placed along the main shaft after the main bearing, INP-A. INP-B is placed as close as possible to the gearbox to minimise the non-torque loads transmitted into the gearbox. INP-B will appear between INP-A and PLC-A
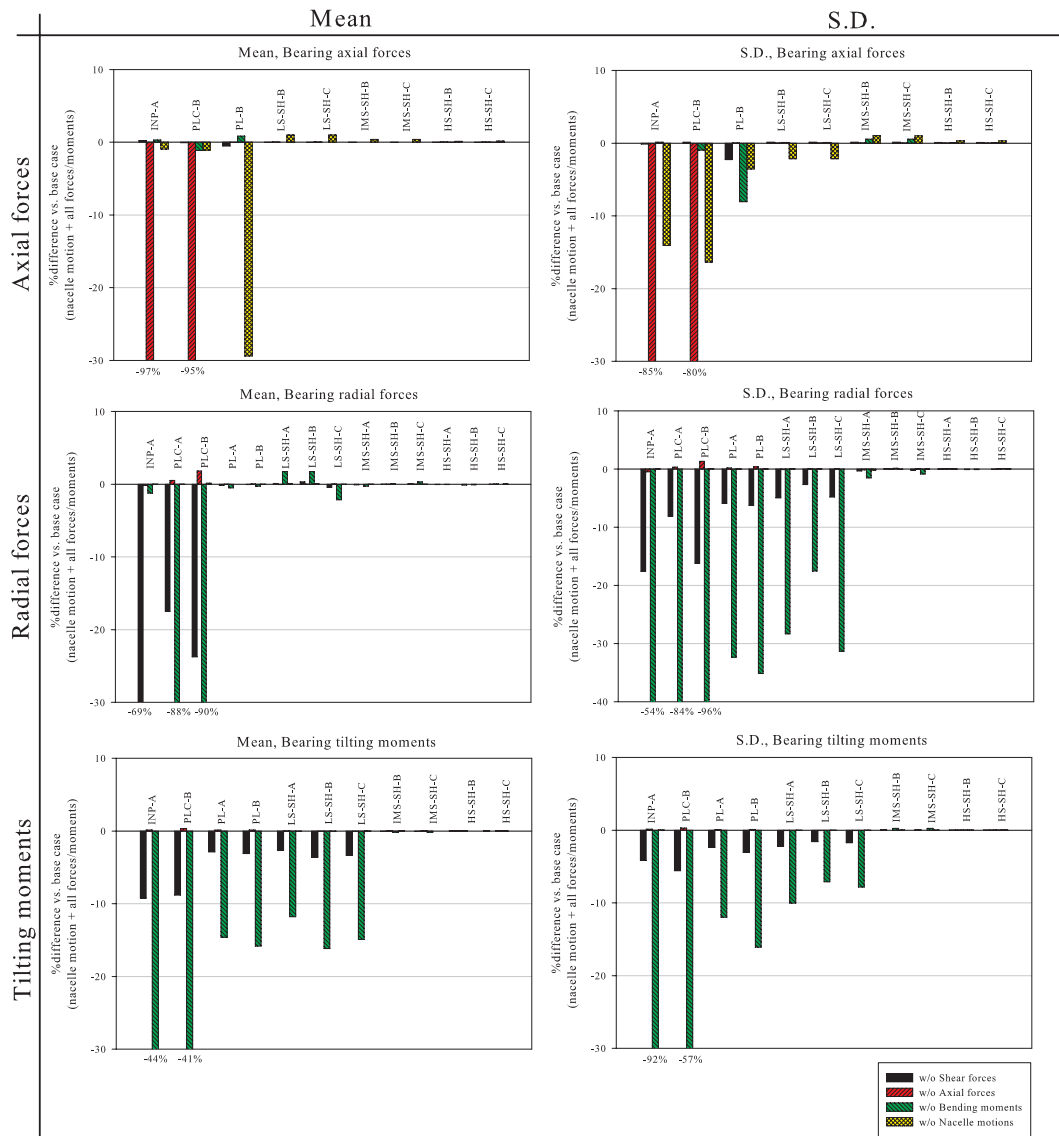
Figure 18. Segregating contributions to the FWT bearing loads.

in the gearbox topology as presented in Figure 3. In the authors' view, this is an effective method as the increases in the internal drivetrain loads are due to the increases in the main shaft non-torque loads (previously discussed in Sections 5 and 6). The results are presented in Tables VII - VIII as the percentage differences of the 4PT versus the 3PT, i.e.

$$\%difference = \frac{X_{4PT} - X_{3PT}}{X_{3PT}} \times 100\%. \tag{10}$$

Only response variables with noticeable differences are presented. Note also that the loads of the 4PT INP-B are compared against the 3PT INP-A loads. Response variables with significant increases are highlighted in the same manner as in Tables III - V.
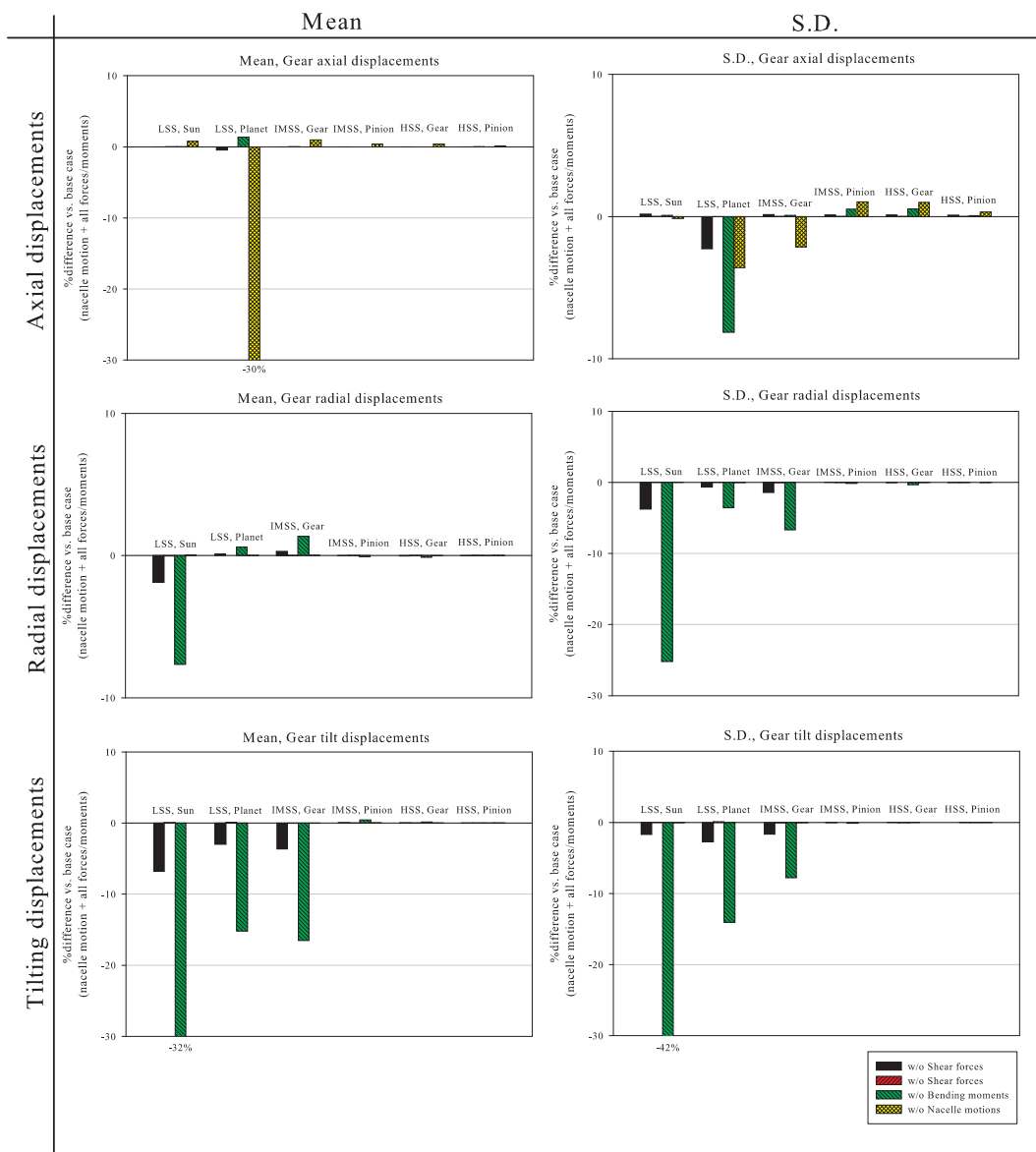
Figure 19. Segregating contributions to the FWT gear displacements.

There are no improvements in the gear contact forces, bearing axial loads of the low speed shaft and bearing loads in the intermediate- and high-speed stages. Otherwise, there are, in general, huge decreases for the 4PT in most of the tooth contact forces and bearing loads presented. These are the response variables associated with the low-speed planetary stage. This coincides with the findings in Section 5 where the response variables associated with the low-speed planetary stage were found to increase the most. It is, therefore, intuitive that any effort to reduce main shaft non-torque loads will also have the most impact at the low-speed planetary stage. The axial forces and tilting moments are also smaller in the 4PT INP-A. This is intuitive as there is now an additional INP-B to carry the main shaft axial loads. Furthermore, the additional INP-B

Table VII. 4PT vs. 3PT. Comparisons of tooth contact forces. Mean values, standard deviations and maximum values.

Gear pair	%difference vs. 3PT											
	Mean				S.D.				Max.			
	LC4	LC5	LC6	LC7	LC4	LC5	LC6	LC7	LC4	LC5	LC6	LC7
LSS-Sun-Planet	0.02	0.01	0.00	0.00	-12.59	-9.73	-1.90	-1.35	-2.06	-2.65	-4.14	2.08
LSS-Planet-Ring	0.02	0.02	0.01	0.01	-12.39	-9.58	-1.90	-1.34	-2.34	-3.25	-3.68	1.08

limits bending in the main shaft, and thus results in less INP-A tilting moments. Also observe that there are increases in the radial bearing loads of INP-A. These increases are relatively substantial, especially in terms of the standard deviations. The improvement in performance using a 4PT in place of a 3PT comes at a cost of an additional main bearing INP-B and a higher grade INP-A bearing. This additional main bearing INP-B is also less lightly loaded as compared to INP-A.

8. CONCLUSIONS

The drivetrain dynamics of a spar-type floating wind turbine (FWT) was studied in this paper. Modelling and simulation of the FWT drivetrain is important to understand its loads and responses, especially in the de-risking of offshore wind turbine designs. The response analysis was carried out in two steps. First, global aero-hydro-elastic-servo analysis was performed in HAWC2 to obtain the loads and motions on the drivetrain. These loads and motions were then used as inputs to a multibody drivetrain model in SIMPACK. A drivetrain model that consisted of six degrees of freedom (dofs) rigid gear wheels with tooth compliance, bearing compliance and flexible shafts was used. The main shaft loads and internal drivetrain responses, which are the tooth contact forces, bearing loads and gear deflections were studied. The investigation was largely based on the comparisons of the mean values, standard deviations and maximum values extrapolated using a 10^{-5} up-crossing rate. Both operational and parked cases were considered. The investigation was performed in three parts. First, the responses were compared between the FWT and its equivalent land-based version (WT). Second, the contributions from the main shaft loads (shear forces, axial forces and bending moments) and nacelle motions to the internal drivetrain responses were individually investigated. Last, a four-point support drivetrain system (4PT) was studied and compared against the original three-point support drivetrain system (3PT). The conclusions are presented below.

FWT versus WT There are general increases in the standard deviations of the main shaft loads and internal drivetrain responses. These increases are larger in the response variables associated with the low-speed planetary stage. This is

Table VIII. 4PT vs. 3PT. Comparisons of bearing loads. Mean values, standard deviations and maximum values. Refer to Figure 3 for bearing notation. * = additional new main bearing.

Bearing	%difference vs. 3PT											
	Mean				S.D.				Max.			
	LC4	LC5	LC6	LC7	LC4	LC5	LC6	LC7	LC4	LC5	LC6	LC7
	Axial forces											
INP-A	-38.29	-38.29	-38.33	-38.40	-39.27	-39.26	-39.23	-38.90	-37.35	-40.17	-40.18	-37.54
INP-B*	-55.79	-55.78	-55.82	-55.77	-96.12	-95.86	-95.08	-94.68	-55.14	-55.00	-54.95	-54.94
PLC-B	-54.72	-54.71	-54.54	-54.53	-54.39	-54.52	-53.97	-53.51	-55.15	-54.25	-55.23	-54.17
PL-B	0.38	0.87	0.74	-0.32	-47.81	-48.90	-43.20	-17.06	-67.04	-67.47	-66.32	-60.93
	Radial forces											
INP-A	11.12	11.44	8.89	6.16	36.09	34.98	35.25	40.57	24.59	24.04	22.09	17.42
INP-B*	-49.25	-51.87	-56.17	-64.27	25.65	21.26	6.19	4.15	-0.25	-7.29	-16.21	-26.41
PLC-A	-99.64	-99.62	-99.45	-99.20	-99.69	-99.68	-99.57	-99.42	-99.66	-99.62	-99.53	-99.44
PLC-B	-91.39	-90.68	-81.82	-68.75	-97.16	-96.98	-94.70	-91.53	-98.24	-97.93	-97.49	-96.74
PL-A	-0.56	-0.59	-0.58	-2.00	-63.94	-61.66	-41.35	-28.18	-34.06	-33.35	-32.81	-32.24
PL-B	-0.47	-0.37	-0.36	0.12	-52.96	-49.80	-28.60	-16.24	-25.42	-26.69	-23.72	-16.29
LS-SH-A	-5.97	-6.13	-7.98	-15.78	-78.41	-76.99	-61.37	-53.80	-40.70	-37.26	-31.32	-24.49
LS-SH-B	2.70	2.57	2.66	5.54	-26.83	-24.50	-8.40	-4.29	-4.70	-5.91	-5.52	-4.57
LS-SH-C	-0.38	-0.26	0.40	2.45	-58.60	-54.15	-27.67	-18.21	-23.25	-23.46	-26.06	-29.42
	Tilting moments											
INP-A	-28.18	-28.28	-28.91	-31.17	-26.45	-26.54	-27.47	-30.83	-27.12	-27.46	-28.00	-30.43
INP-B*	-95.94	-95.83	-95.29	-94.61	-98.86	-98.85	-98.78	-98.85	-98.39	-98.25	-97.91	-97.61
PLC-B	-88.45	-88.16	-86.95	-86.12	-91.28	-91.08	-90.32	-90.38	-94.69	-94.20	-93.23	-92.84
PL-A	-22.11	-21.38	-24.20	-48.16	-21.03	-20.32	-24.58	-48.73	-19.77	-18.12	-14.90	-12.64
PL-B	-24.40	-23.49	-25.80	-47.36	-28.00	-26.74	-29.27	-49.28	-31.64	-29.77	-24.69	-20.86
LS-SH-A	-24.88	-24.38	-27.42	-42.78	-41.44	-40.94	-47.00	-71.40	-15.32	-14.81	-12.35	-13.57
LS-SH-B	-40.88	-40.31	-45.51	-63.00	-38.82	-38.45	-43.55	-68.08	-23.69	-23.10	-18.45	-19.14
LS-SH-C	-38.73	-38.21	-44.37	-65.77	-40.83	-40.46	-44.73	-67.08	-26.23	-25.07	-23.57	-31.24

Prepared using weauth.cls

intuitive as the gearbox has the capability to isolate loads between individual stages. These differences, however, do also propagate to the intermediate- and high-speed stage at the less severe load cases. The increases in the maximum values, on the other hand, are primarily limited to the low-speed planetary stage. Comparisons of the frequency spectra show that wave-induced responses appear both in the main shaft loads and internal drivetrain response variables.

Contributions of individual main shaft loads and nacelle motions Main shaft non-torque loads are very important in the prediction of accurate internal drivetrain responses, in particular for the bearing loads and gear displacements. Nacelle motions, i.e. inertia loads, on the other hand, do not have significant contributions to most response variables, except the bearing axial forces in the low-speed planetary stage and planet gear axial displacements. This gives the further conclusion that the differences in the FWT and WT in terms of the internal drivetrain responses are a result of the differences in the main shaft non-torque loads experienced. Main shaft non-torque load and nacelle motions have limited contributions at the intermediate- and high-speed stages. It is mentioned again that the nacelle motions referred here are the motions applied in the SIMPACK multi-body model, and were calculated from the global aero-hydro-elastic-servo simulations performed in HAWC2.

Four-point support system It was found that the 4PT when applied to a FWT drivetrain significantly reduces tooth contact forces and bearing loads in the low-speed planetary stage. This, however, comes at the expense of increased main bearing radial loads, especially in terms of standard deviations.

ACKNOWLEDGEMENTS

REFERENCES

1. Jonkman J. Dynamic modelling and loads analysis of an offshore floating wind turbine. *Technical Report*, National Renewable Energy Laboratory 2007.

2. Sclavounos P, Tracy C, Lee S. Floating offshore wind turbines: responses in a seastate pareto optimal designs and economic assessment. *ASME 2008 27th International Conference on Offshore Mechanics and Arctic Engineering*, Estoril, Portugal, 2008.

3. Karimirad M, Gao Z, Moan T. Dynamic motion analysis of catenary moored spar wind turbine in extreme environmental condition. *Offshore Wind Conference 2009, Stockholm, Sweden*, 2009.

4. Skaare B, Hanson TD, Nielsen FG, Yttervik R, Hansen AM, Thomsen K, Larsen T. Integrated dynamic analysis of floating offshore wind turbines. *European Wind Energy Conference*, Milan, Italy, 2007.

5. Jonkman J. Definition of the floating system for phase IV of OC3. *Technical Report*, National Renewable Energy Laboratory 2010.

6. Karimirad M, Moan T. Extreme structural dynamic response of a spar type wind turbine. *International Conference on Ocean, Offshore and Arctic Engineering, China*, 2010.

7. Karimirad M. Stochastic dynamic response analysis of spar-type wind turbines with catenary or taut mooring systems. PhD Thesis, Norwegian University of Science and Technology, Trondheim, Norway 2011.

8. Karimirad M, Moan T. Wave and wind induced dynamic response of a spar-type offshore wind turbine. *Journal of Waterway, Port, Coastal, and Ocean Engineering* 2012; **138**(1):9–20.

9. Karimirad M, Moan T. Extreme dynamic structural response analysis of catenary moored spar wind turbine in harsh environmental conditions. *Journal of Offshore Mechanics and Arctic Engineering, ASME* 2011; **133**(4):041 103.

10. Peeters JLM, Vandepitte D, Sas P. Flexible multibody model of a three-stage planetary gearbox. *International Conference on Noise and Vibration Engineering*, Leuven, Belgium, 2004.

11. Peeters JLM, Vandepitte D, Sas P. Analysis of internal drive train dynamics in a wind turbine. *Wind Energy* 2006; **9**(1-2):141–161.

12. Peeters JLM. Simulation of dynamic drive train loads in a wind turbine. PhD Thesis, Department of Mechanical Engineering, Katholieke Universiteit Leuven 2006.

13. Oyague F, Gorman D, Sheng S. Progressive dynamical drive train modeling as part of nrel gearbox reliability collaborative. *Windpower 2008 Conference and Exhibition*, Houston, Texas, 2008.

Prepared using weauth.cls

14. Oyague F. Gearbox modeling and load simulation of a baseline 750-kW wind turbine using state-of-the-art simulation codes. *Technical Report*, National Renewable Energy Laboratory 2009.

15. Oyague F, Butterfield CP, Sheng S. Gearbox reliability collaborative analysis round robin. *American Wind Energy Association Windpower 2009 Conference*, Chicago, Illinois, 2009.

16. Oyague F, Gorman D, Sheng S. Nrel gearbox reliability collaborative experiment data overview and analysis. *Windpower 2010 Conference and Exhibition*, Dallas, Texas, 2010.

17. Helsen J, Heirman G, Vandepitte D, Desmet W. The influence of flexibility within multibody modelling of multi-megawatt wind turbine gearboxes. *International Conference on Noise and Vibration Engineering, Leuven, Belgium*, 2008.

18. Helsen J, Vanhollebeke F, De Coninck F, Vandepitte D, Desmet W. Insights in wind turbine drive train dynamics gathered by validating advanced models on a newly developed 13.2 MW dynamically controlled test-rig. *Mechantronics* 2011; **21**(4):737–752.

19. Helsen J, Vanhollebeke F, Marrant B, Vandepitte D, Desmet W. Multibody modelling of varying complexity for modal behaviour analysis of wind turbine gearboxes. *Renewable Energy* 2011; **36**(11):3098–3113.

20. Helsen J, Vanhollebeke F, Vandepitte D, Desmet W. Optimized inclusion of flexibility in wind turbine gearbox multibody model in view of model updating on dynamic test rig. *The 1st Joint International Conference on Multibody System Dynamics, Lapppeenranta, Finland*, 2011.

21. Xing Y, Moan T. Wind turbine gearbox planet carrier modelling and analysis in a multibody setting. *Wind Energy Journal (accepted)* 2012; .

22. Xing Y, Karimirad M, Moan T. Effect of spar-type floating wind turbine nacelle motion on drivetrain dynamics. *European Wind Energy Association (EWEA) Annual Event*, Copenhagen, Denmark, 2012.

23. Link H, LaCava W, van Dam J, McNiff B, Sheng S, Wallen R, McDade M, Lambert S, Butterfield S, Oyague F. Gearbox reliability collaborative project report: findings from phase 1 and phase 2. *Technical Report*, National Renewable Energy Laboratory 2011.

24. Koo BJ, Jim MH, Randal RE. Mathieu instability of a spar platform with mooring and risers. *Ocean Engineering* 2004; **31**(17-18):2175–2208.

25. Ormberg H, Mo K. Simo - user's manual version 3.6. *Technical Report*, MARINTEK 2009.

26. Ormberg H, Passano E. Riflex - user's manual version 3.6. *Technical Report*, MARINTEK 2009.

27. Karimirad M, Moan T. A simplified method for coupled analysis of floating offshore wind turbines. *Marine Structures* 2012; **27**(1):45–63.

28. Gao Z, Luan C, Moan T, Bjrn S, Solberg T, Lygren J. Comparative study of wind and wave induced dynamic responses of three floating wind turbines supported by spar, semi-submersible and tension-leg floaters. *International Conference on Offshore Wind Energy and Ocean Energy, Beijing, China*, 2011.

29. Kvittem MI, Moan T, Gao Z, Luan C. Short-term fatigue analysis of semi-submersible wind turbine tower. *ASME 30th International Conference on Ocean, Offshore and Arctic Engineering, Rotterdam, The Netherlands*, 2011.

30. Larsen TJ. *How 2 HAWC2*. Risoe National Laboratory, Technical University of Denmark, Roskilde 2009.

31. *SIMPACK*. Available from: http://www.simpack.com.

32. Larsen TJ, Hanson TD. A method to avoid negative damped low frequent tower vibrations for a floating, pitch controlled wind turbine. *The Science of Making Torque from Wind, Lyngby, Denmark*, 2007.

33. Xing Y, Pedersen E, Moan T. An inertia-capacitance beam substructure formulation based on the bond graph method with application to rotating beams. *Journal of Sound and Vibrations* 2011; **330**(21):5114–5130.

34. Wu CH, Haug EJ. Geometric non-linear substructuring for dynamics of flexible mechanical systems. *International Journal for Numerical Methods in Engineering* 1988; **26**(10):2211–2226.

35. Hansen MH, Gaunaa M, Madsen HA. A beddoes-leishman type dynamic stall model in state-space and indicial formulations. *Technical Report*, Risoe National Laboratory 1984.

36. Glauert H. *Aerodynamic Theory*, vol. 4, chap. L: Airplane propellers. Julius Springer: Berlin, Germany, 1935.

37. Faltinsen OM. *Sea loads on ships and offshore structures*. 1st ed. edn., Cambridge University Press, Cambridge: Cambridge, UK, 1990.

38. Karimirad M, Meissonnier Q, Moan T. Hydro-elastic code-to-code comparison for a tension leg spar type floating wind turbine. *Marine Structures* 2011; **24**(4):412–435.

39. *ISO 6336-1:2006: Calculation of load capacity of spur and helical gears – Part 1: Basic principles, introduction and general influence factors*. 2nd ed. edn. 2006.

40. Johannessen K, Meling TS, Haver S. Joint distribution for wind and waves in the northern north sea. *11th Internation Offshore and Polar Engineering Conference, Stavanger, Norway*, 2001.

41. *ISO 61400-3:2009: Design requirements for offshore wind turbines*. 1st ed. edn. 2009.

42. Mann J. Models in micrometeorology. *Technical Report*, Risoe National Laboratory 1994.

43. Mann J. The spatial structure of neutral atmospheric surface-layer turbulence. *Journal of Fluid Mechanics* 1994; **273**(1):141–168.

44. Naess A, Gaidai O, Teigen PS. Extreme response prediction for nonlinear floating offshore structures by monte carlo simulation. *Applied Ocean Research* 2007; **29**(4):221–230.

45. LaCava W, Xing Y, Guo Y, Moan T. Determining wind turbine gearbox model complexity using measurement validation and cost comparison. *European Wind Energy Association (EWEA) Annual Event*, Copenhagen, Denmark, 2012.

APPENDIX - MODEL FIDELITY STUDY

The model fidelity study from Xing et al. [22] is presented here. The study looked at three drivetrain models with increasing levels of model fidelity. The model descriptions are presented in Table IX. The motivation is to investigate the level of model detail required to converge on the statistical responses of the internal drivetrain responses. The FWT LC4 case (refer to Table II) is used for this study. The results are presented in Figures 20 - 22 as the percentage difference versus the GB03 model. Bearing loads below 100 N or 100 Nm are not presented. A zero per cent difference in a particular response variable means that the indicated model, i.e., GB01 or GB02 is able to produce the same result as GB03. The results from the model fidelity study show that the GB02 model (red and yellow bars) is sufficient for reasonable convergence of most internal drivetrain responses, i.e. tooth contact forces and bearing loads, and thus used in this paper. Notice that most of the axial gear displacements require a very high fidelity model, i.e., GB03, to reasonably converge well. It is, however, not practical to use the GB03 models due to the high computational costs involved. As a reference, the GB01, GB02 and GB03 models require one, three and seven days of computational time for an one-hour simulation, respectively.

Table IX. Drivetrain models used in the model fidelity study in Xing et al. [22]

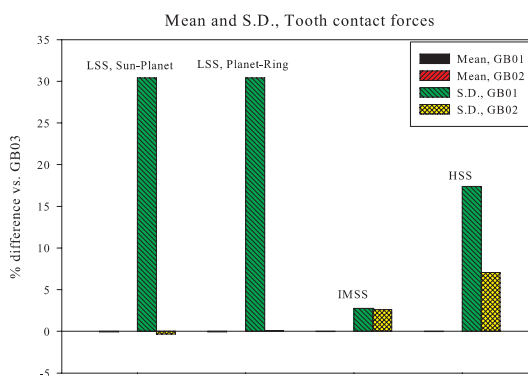| Model	Description
GB01	Six DOF rigid gear wheels with tooth compliances and bearing compliances.
GB02	GB01 with addition of shaft compliances.
GB03	GB02 with addition of flexible planet carrier, gearbox housing and torque arms support compliances.

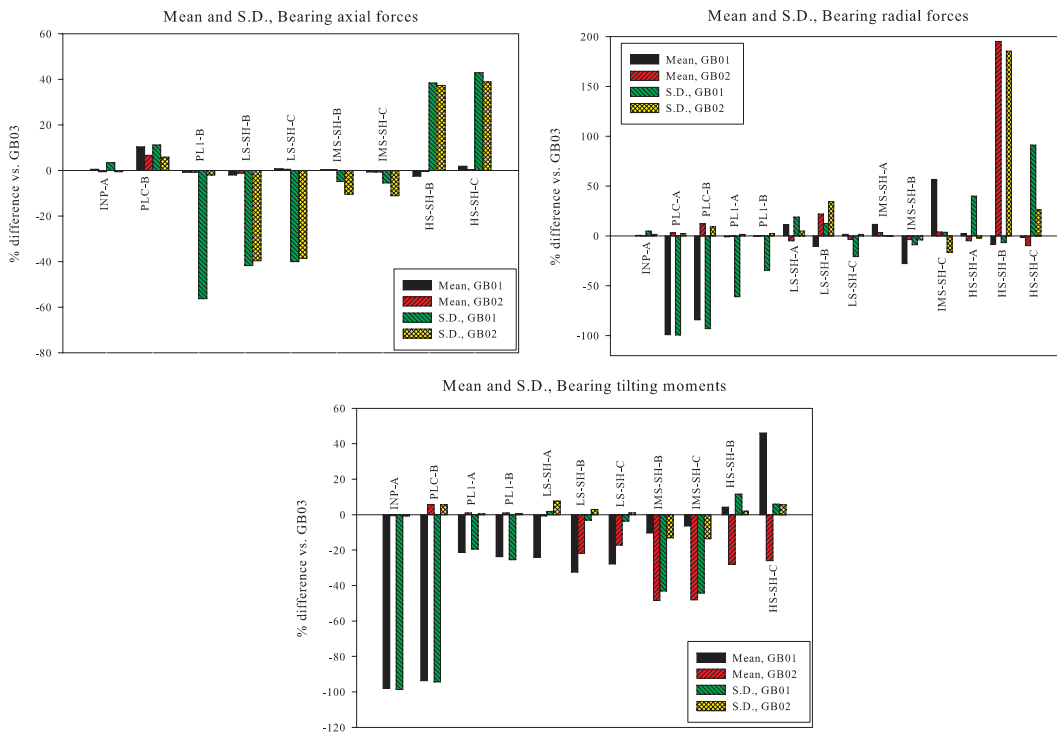**Figure 20.** Comparison of tooth contact forces from the GB01, GB02 and GB03 models.

Figure 21. Comparison of bearing loads from the GB01, GB02 and GB03 models.
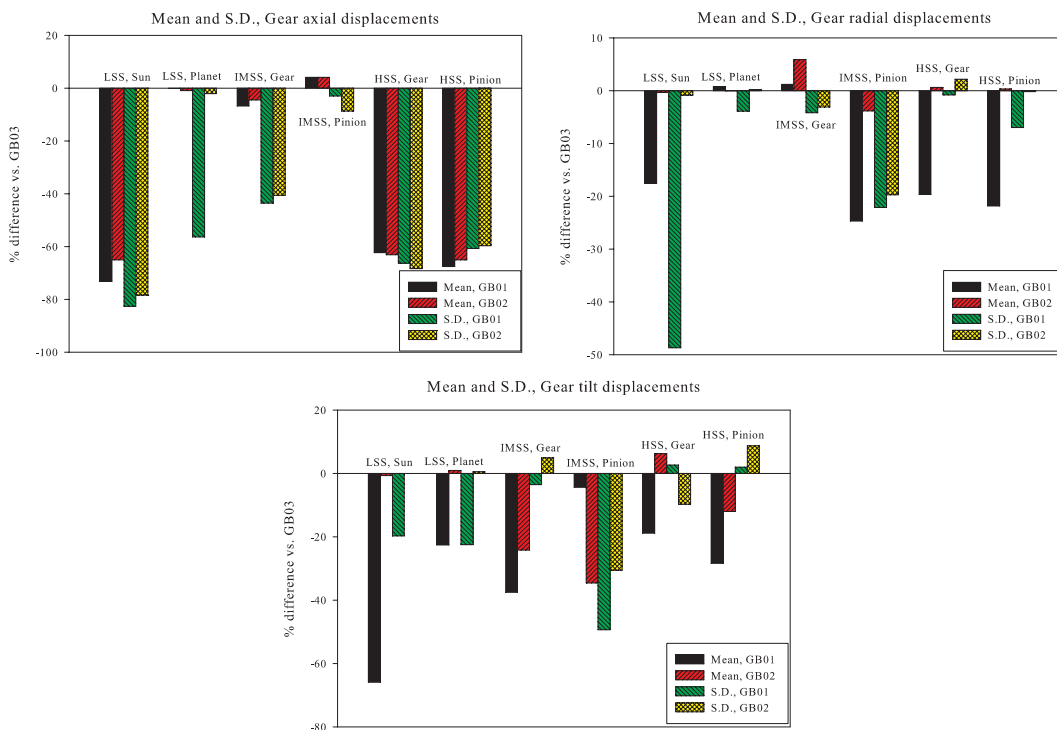

Figure 22. Comparison of gear displacements from the GB01, GB02 and GB03 models.